

# Complex dispersion lines in gapped bilayer graphene: Analytical expressions and shear-displacement effects on monolayer–bilayer–monolayer junction conductance

Ryo Tamura

Faculty of Engineering, Shizuoka University, 3-5-1 Johoku, Hamamatsu 432-8561, Japan

(Dated: February 25, 2026)

Analytical treatments of tunneling in bilayer graphene have typically relied on minimal models including only the vertical interlayer hopping  $\gamma_1$  and have been restricted to the weak interlayer bias regime  $2\varepsilon \ll \gamma_1$ . These simplifications limit the ability of analytical theories to describe lattice deformations and strong electric-field effects. In this work, we present an analytical theory of evanescent states in electrically gapped bilayer graphene that overcomes both limitations. Specifically, our approach explicitly incorporates the skew interlayer hoppings  $\gamma_3$  and  $\gamma_4$  and remains valid even when the interlayer bias  $2\varepsilon$  is comparable to  $\gamma_1$ . Focusing on low-energy electronic states near the charge neutrality point, we analytically derive the complex longitudinal wave numbers, the gap width, and the sublattice pseudospin inside the electric-field-induced gap, and systematically analyze their dependence on the interlayer shear displacement  $\vec{\delta} = (\delta_x, \delta_y)$ . The analytical expressions quantitatively reproduce exact numerical calculations, demonstrating that skew interlayer hoppings, in particular  $\gamma_3$ , play an essential role. Taking the zigzag direction as the longitudinal (transport)  $x$  direction, the wave vector becomes complex along  $x$  while remaining real along the transverse  $y$  direction. For a monolayer–bilayer–monolayer junction with transport along this direction, we find that  $\delta_y$  has a significantly stronger impact on the conductance than  $\delta_x$ . This anisotropic response is quantitatively explained by the analytical expressions. Furthermore, we identify a shear-induced phase proportional to  $\delta_y$  that appears universally in the analytical expressions for the gap width, the sublattice pseudospin, and the decay length. These results establish a unified analytical framework for shear- and bias-controlled evanescent tunneling in bilayer graphene and suggest broader relevance to nonequilibrium transport phenomena in layered materials.

## I. INTRODUCTION

Quantum transport across heterojunctions is governed not only by propagating states but also by evanescent modes, whose complex wave vectors determine tunneling amplitudes and decay lengths inside barrier regions [1–6]. A representative system that exploits this property is the monolayer–bilayer–monolayer (mono–bi–mono) graphene junction, where AB-stacked bilayer graphene forms the central region, while the outer monolayer regions act as source and drain leads, as illustrated in Fig. 1(a) and 1(b). Because a perpendicular electric field opens an energy gap exclusively in the central bilayer region, the junction realizes an atomically sharp tunneling barrier. The barrier height is determined by the gap width and can be controlled *in situ* via the applied electric field [7–14]. Numerous theoretical studies have investigated the conductance of such mono–bi–mono junctions within the Landauer formalism [15–33]. However, most analytical approaches are restricted to the regime where the electrically induced gap is small compared with the vertical interlayer hopping  $\gamma_1$ . When the gap width becomes comparable to  $\gamma_1$  and the Fermi level lies inside the gap, conventional low-energy reductions break down and analytical treatments become scarce [5, 6, 34]. While reduced two-band descriptions have proven useful in moiré graphene systems and related gauge-field analyses, these approaches typically focus on low-energy mini-band physics [36–42]. In contrast, the present problem involves evanescent states inside an electrically induced gap comparable to  $\gamma_1$ , where the full four-band structure

becomes essential. Although Refs. [15] and [16] addressed this parameter regime, the effect of interlayer shear displacement on conductance was not the primary focus and was treated mainly numerically, so that its microscopic origin remained unclear. Clarifying this issue is one of the central aims of the present work.

Interlayer shear vibrations in bilayer and few-layer graphene have been observed experimentally by Raman spectroscopy and time-resolved optical measurements, demonstrating low-frequency shear phonon modes and their dependence on the number of layers [43–45]. Despite these experimental advances, analytical descriptions of the associated electronic effects remain relatively limited compared with the well-developed theory of intralayer strain, where lattice deformations can be described as effective gauge fields within continuum Dirac models [46–50]. While this gauge-field framework has clarified the microscopic origin of electron–phonon coupling in monolayer graphene, interlayer shear displacements in bilayer systems have been explored far less extensively, especially when a large electric-field-induced energy gap is present [51, 52]. First-principles calculations have examined the relationship between the gap width and shear displacement; however, the underlying physical origin has not yet been clarified [53].

It is also worth noting that a variety of one-dimensional electronic states inside the bulk energy gap of graphene-based systems have been extensively studied, including edge states [54–59] and domain-wall states, where the domain walls arise from differences in perpendicular electric fields [60–67], interlayer stacking [68–73], or sublattice

tice site energies [74, 75]. These states propagate along specific interfaces and are often protected by topology or symmetry. In contrast, the present work focuses on evanescent bulk states inside the gap, which do not form real dispersion lines (RDLs) but instead govern tunneling and decay processes across gapped regions. The electronic structure of such evanescent states is naturally described in terms of complex dispersion lines (CDLs), in which the real and imaginary parts of the wave vector encode oscillatory and decaying behavior, respectively. While CDLs have been extensively studied in conventional semiconductor heterostructures [3, 4], systematic analyses of CDLs in graphene-based junctions have mostly been restricted to models neglecting the skew interlayer hoppings  $\gamma_3$  and  $\gamma_4$ . These skew hoppings play a more significant role than the vertical hopping  $\gamma_1$  in determining the influence of interlayer shear displacement on the CDL.

In this work, we investigate the complex dispersion lines (CDLs) of AB-stacked bilayer graphene under a perpendicular electric field using a tight-binding model that fully incorporates the interlayer hopping parameters and interlayer shear displacement. We focus on low-energy electronic states near the charge neutrality point while allowing for a large interlayer bias comparable to the dominant interlayer hopping. We derive approximate analytical expressions for the CDLs that accurately reproduce exact numerical results over a wide energy range inside the gap and clarify their physical origin in terms of shear-modified interlayer coupling. These results are then applied to analyze electron transmission across mono-bi-mono junctions, where the shear-induced modification of the decay length directly controls the conductance. Finally, we discuss a possible experimental setup in which dynamically driven shear displacement, combined with an external probe field, may generate a dc current, providing a direct way to explore nonequilibrium tunneling governed by evanescent states and offering further insight into tunneling transport in shear-displaced bilayer graphene.

## II. TIGHT BINDING MODEL AND $\lambda$ - $(\lambda^*)^{-1}$ SYMMETRY

We use  $\pi$  orbital tight binding (TB) model with the standard notation of hoppings,  $(\gamma_0, \gamma_1, \gamma_3, \gamma_4)$ . The intralayer nearest-neighbor hopping  $\gamma_0$  is negative, with  $\gamma_0 = -|\gamma_0| = -1 = -3.12$  eV. Unless otherwise noted, we adopt units where  $|\gamma_0| = 1$ . Figure 2 (a) and (b) show the wave function amplitudes  $(\circ_+, \bullet_+, \circ_-, \bullet_-)\lambda^{j_x}\omega^{j_y}$  with integers  $j_x, j_y$ , Bloch factors  $\lambda = \exp(ik_x a/2)$ ,  $\omega = \exp(3k_y b/2)$ , lattice constant  $a = 0.246$  nm, and bond length  $b = a/\sqrt{3}$ . The interlayer hopping is multiplied by factors  $\exp(-\Delta r/L_c)$ , where  $L_c = 0.045$  nm, and  $\Delta r$  denotes the change in interatomic distance induced by the shear displacement  $\vec{\delta} = (\delta_x, \delta_y)$  of layer  $-$  relative to

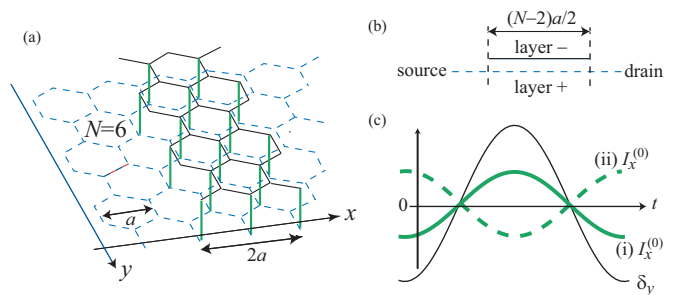


FIG. 1. (a) Schematic three-dimensional view and (b) side view of a mono-bi-mono junction. A layer  $-$  of length  $(N-2)a/2$  is AB-stacked and interlayer-coupled to a layer  $+$  connecting the source and drain electrodes, where  $N$  is an integer and  $a$  is the lattice constant. (c) Conceptual illustration of a pump-probe scheme: a  $y$ -polarized pump field, independently controlled and arriving first, induces a shear displacement  $\delta_y$  along the  $y$  direction, while a delayed, independently controlled  $x$ -polarized probe field induces the probability current  $I_x^{(0)}$  along the  $x$  direction for electrons incident from the monolayer region. Cases where  $\delta_y$  and  $I_x^{(0)}$  are (i) in phase and (ii) out of phase are shown. The horizontal axis represents time  $t$ . See Sec. VIII for details.

layer  $+$  [76]. More explicitly,

$$\gamma_1 = \gamma_1^{(0)} e^{(r_0 - \tilde{r}_0)/L_c} \quad (1)$$

for the vertical  $\circ_+ - \circ_-$  hopping,

$$\gamma_4^{(y)} = \gamma_4^{(0)} e^{(r_1 - \sqrt{r_1^2 + 2b\delta_y})/L_c} \quad (2)$$

for the skew hopping in the  $y$  direction ( $j_y \rightarrow j_y \pm 1$ ), and

$$\gamma_3^{(\varsigma x)} = \gamma_3^{(0)} e^{(r_1 - \sqrt{\tilde{r}_1^2 \pm b\delta_y + \varsigma a\delta_x})/L_c} \quad (3)$$

for the skew hopping in the  $x$  direction ( $j_x \rightarrow j_x + \varsigma 1$ ), where  $r_0$  denotes the interlayer distance ( $r_0 = 0.335$  nm),  $\varsigma = \pm$ ,  $r_1 = \sqrt{r_0^2 + b^2}$ ,  $\tilde{r}_0 = \sqrt{r_0^2 + |\vec{\delta}|^2}$ ,  $\tilde{r}_1 = \sqrt{r_1^2 + |\vec{\delta}|^2}$ ,  $\gamma_1^{(0)} = 0.377$  eV,  $\gamma_3^{(0)} = 0.29$  eV, and  $\gamma_4^{(0)} = 0.12$  eV [77]. Here, the positive direction of  $\delta_y$  corresponds to the orientation where the angle between the  $\gamma_1$  bond and the in-plane  $\gamma_0$  bond on the  $yz$  plane is obtuse.

The tight-binding equation reads

$$H \begin{pmatrix} \vec{\chi}_+ \\ \vec{\chi}_- \end{pmatrix} = E \begin{pmatrix} \vec{\chi}_+ \\ \vec{\chi}_- \end{pmatrix}, \quad (4)$$

where  ${}^t\vec{\chi}_\pm = (\circ_\pm, \bullet_\pm)$  denotes the layer-resolved wave function. We write the Hamiltonian in the block form

$$H = \begin{pmatrix} h_{+,+} - \varepsilon & h_{+,-} \\ h_{-,+} & h_{-,-} + \varepsilon \end{pmatrix}, \quad (5)$$

with interlayer site energy difference  $2\varepsilon$ , and the explicit form of each block is

$$h_{\pm,\pm} = \begin{pmatrix} 0 & (1 - \xi)\omega^{\pm 1} - 1 \\ (1 - \xi)\omega^{\mp 1} - 1 & 0 \end{pmatrix}, \quad (6)$$

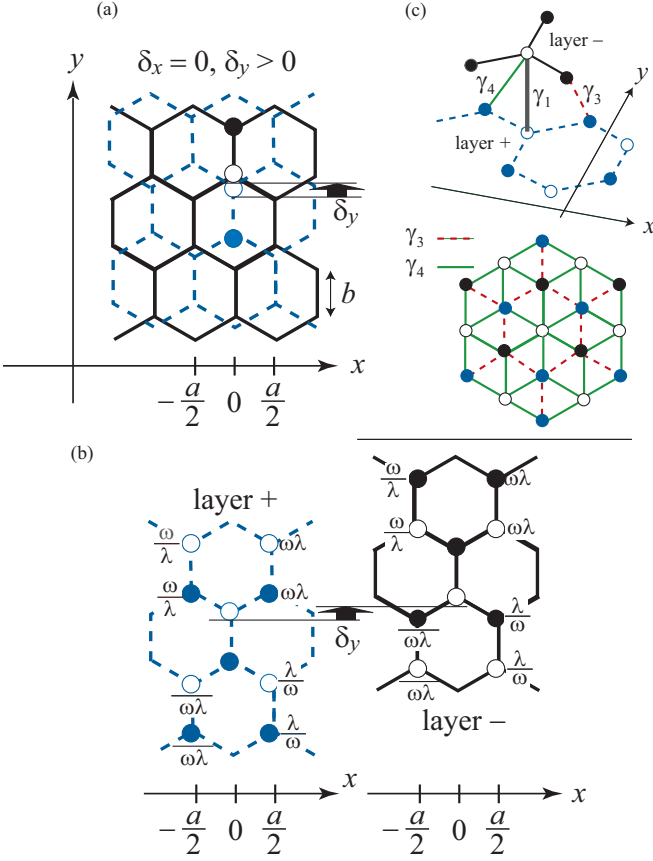


FIG. 2. Atomic positions are labeled by integers  $j_x$  and  $j_y$  along the  $x$  and  $y$  directions. The vector  $\vec{\delta} = (\delta_x, \delta_y)$  denotes the shear displacement of layer  $-$  relative to layer  $+$ . (a) Wave-function amplitudes ( $\circ_+, \bullet_+, \circ_-, \bullet_-$ ) at  $j_x = j_y = 0$  for  $\delta_x = 0$  and  $b \gg \delta_y > 0$ . The layer index  $\pm$  is suppressed for clarity, and  $b = a/\sqrt{3}$  is the in-plane bond length. Dashed and solid lines denote layer  $+$  and layer  $-$ , respectively. (b) Wave-function amplitudes ( $\circ, \bullet$ )  $\lambda^{j_x} \omega^{j_y}$  in each layer for  $|j_x| \leq 1$  and  $|j_y| \leq 1$ . (c) Interlayer hopping parameters  $\gamma_1$ ,  $\gamma_3$ , and  $\gamma_4$ . The top panel shows a schematic three-dimensional view, while the bottom panel shows a projection onto the  $(x, y)$  plane for  $\delta_x = \delta_y = 0$ .

$$h_{\mp, \pm} = \begin{pmatrix} \gamma_1 & f_4^{(\pm)} \\ f_4^{(\pm)} & f_3^{(\pm)} \end{pmatrix}, \quad (7)$$

$$f_3^{(\pm)} \equiv \gamma_3^{(y)} \omega^{\pm 2} + \left[ \tilde{\gamma}_3^{(x)} (\xi - 1) \mp \widehat{\gamma}_3 \eta \right] \omega^{\pm 1}, \quad (8)$$

and

$$f_4^{(\pm)} \equiv \gamma_4^{(y)} + \left[ \tilde{\gamma}_4^{(x)} (\xi - 1) \mp \widehat{\gamma}_4 \eta \right] \omega^{\pm 1}. \quad (9)$$

The parameters  $\xi$  and  $\eta$  are determined by the Bloch factor  $\lambda$  as

$$\xi \equiv \lambda + \frac{1}{\lambda} + 1 \quad (10)$$

and

$$\eta \equiv \frac{1}{2} \left( \lambda - \frac{1}{\lambda} \right). \quad (11)$$

The definitions

$$\tilde{\gamma}_{3,4}^{(x)} \equiv \frac{1}{2} \left( \gamma_{3,4}^{(+x)} + \gamma_{3,4}^{(-x)} \right) \quad (12)$$

and

$$\widehat{\gamma}_{3,4} \equiv \gamma_{3,4}^{(+x)} - \gamma_{3,4}^{(-x)} \quad (13)$$

represent the average and the difference of  $x$ -shifted skew hoppings, respectively. Note that  $\widehat{\gamma}_{3,4} \delta_x < 0$ , which will be important later. In the effective theory, the wave number measured from the  $K$  and  $K'$  valley points is defined as  $\tilde{k}_x = k_x \pm 4\pi/(3a)$ . Appendix A proves that it is related to Eq. (10) via  $\tilde{k}_x a = \pm 2\xi/\sqrt{3}$  [78, 79]. Since we consider the case where  $|\varepsilon| \ll 1$  and  $|E| \ll 1$ ,  $\xi$  and  $\tilde{k}_x$  are close to zero.

The secular equation

$$\det(E - H) = 0 \quad (14)$$

is equivalent to

$$\det(E - {}^t H^*) = 0, \quad (15)$$

where  $H$  is defined in Eq. (5). When  $|\lambda| \neq 1$ ,  $H$  is not a Hermitian matrix, and hence  $H \neq {}^t H^*$ . Replacing  $H$  with  ${}^t H^*$  is equivalent to replacing  $\lambda$  with  $(\lambda^*)^{-1}$ . In other words, if  $\lambda$  is an allowed Bloch factor, then  $(\lambda^*)^{-1}$  is also allowed for the same value of  $k_y$ . We refer to this property as the  $\lambda - (\lambda^*)^{-1}$  symmetry. Note that  $E$ ,  $\varepsilon$ , and  $k_y$  are common to Eqs. (14) and (15). This symmetry originates from the translational periodicity along the  $x$  axis. The  $\lambda - (\lambda^*)^{-1}$  symmetry simplifies the analysis with respect to  $\lambda$  in the following ways: (i) It is sufficient to consider only the case  $|\lambda| < 1$ . Its partner  $\frac{1}{\lambda^*}$  corresponds to a Bloch factor whose magnitude is greater than unity. (ii) When we explicitly indicate that  $k_y$  is fixed in Eqs. (14) and (15), the  $\lambda - (\lambda^*)^{-1}$  symmetry can be written as the  $\lambda(k_y) - (\lambda^*(k_y))^{-1}$  symmetry. Time-reversal symmetry guarantees the  $\lambda(k_y) - \lambda^*(-k_y)$  symmetry, but it does not guarantee the  $\lambda(k_y) - \lambda^*(k_y)$  symmetry. However, when  $\delta_x = 0$ , the system possesses the  $\lambda(k_y) - (\lambda(k_y))^{-1}$  symmetry; combining this with the  $\lambda(k_y) - (\lambda^*(k_y))^{-1}$  symmetry allows us to establish the  $\lambda(k_y) - \lambda^*(k_y)$  symmetry. Therefore, when  $\delta_x = 0$ , it is sufficient to present  $\lambda(k_y)$  for a single valley even when  $k_y \neq 0$ . Both valleys need to be shown only when  $\delta_x k_y \neq 0$ .

### III. $\tilde{\Delta}\xi$ APPROXIMATION

Equations (10) and (11) can be rewritten as

$$\lambda^{(\sigma)} = \frac{\xi - 1}{2} + \sigma \sqrt{\left( \frac{\xi - 1}{2} \right)^2 - 1}, \quad (16)$$

and

$$\eta = \sigma \sqrt{\left(\frac{\xi - 1}{2}\right)^2 - 1}, \quad (17)$$

where  $\sigma = \pm$ . When  $k_y \delta_x \neq 0$ , the  $\lambda$ - $\lambda^{-1}$  symmetry is absent, and hence  $\lambda^{(+)}\lambda^{(-)} \neq 1$ . This is because the secular equation (14) depends not only on  $\xi$  but also on  $\eta$ , so that the solution  $\xi$  satisfying Eq. (14) depends on  $\sigma$  as well. We use the notations  $A^r = \text{Re}(A)$  and  $A^i = \text{Im}(A)$  for the real and imaginary parts of a complex number  $A$ , respectively, and define  $\text{sgn}(B) = B/|B|$  for a real number  $B$ . Equation (16) is approximated as

$$\lambda^{(\sigma)} \simeq \exp\left(\sigma \left[-\frac{|\xi^i|}{\sqrt{3}} + i \text{sgn}(\xi^i) \left(\frac{\xi^r}{\sqrt{3}} - \frac{2}{3}\pi\right)\right]\right) \quad (18)$$

for a nonzero  $\xi^i$ , and

$$\lambda^{(\sigma)} \simeq \exp\left[\sigma i \left(\frac{\xi}{\sqrt{3}} - \frac{2}{3}\pi\right)\right] \quad (19)$$

for  $\xi^i = 0$ . See Appendix A for the derivation. When  $|\lambda| = 1$ , Eq. (19) shows that  $\sigma$  serves as the valley index. Owing to the  $\lambda$ - $(\lambda^*)^{-1}$  symmetry, the discussion can be restricted to the case  $|\lambda| \leq 1$ . When  $|\lambda| \neq 1$ , we choose  $\sigma = +$  according to this restriction and abbreviate  $\lambda^{(+)}$  as  $\lambda$ .

We introduce  $X = \det(E - H)$  and regard the equation  $X = 0$  as an equation for determining  $\xi$ . When  $\gamma_3 = \gamma_4 = 0$ , the exact solution for  $\xi$  is given by

$$\xi_{\tau,l}^{(0)} = 1 - c - \tau \sqrt{p - s^2 + ilq} \quad (20)$$

where  $\tau = \pm$ ,  $l = \pm$ ,  $s \equiv \sin(\frac{3}{2}k_y b)$ ,  $c \equiv \cos(\frac{3}{2}k_y b)$ ,  $p \equiv E^2 + \varepsilon^2$ ,

$$q \equiv \begin{cases} \sqrt{\varepsilon^2 \gamma_1^2 - (4\varepsilon^2 + \gamma_1^2)E^2} \dots & |E| < \frac{|\varepsilon \gamma_1|}{\sqrt{4\varepsilon^2 + \gamma_1^2}} \\ -i\sqrt{(4\varepsilon^2 + \gamma_1^2)E^2 - \varepsilon^2 \gamma_1^2} \dots & |E| > \frac{|\varepsilon \gamma_1|}{\sqrt{4\varepsilon^2 + \gamma_1^2}} \end{cases}. \quad (21)$$

When  $\xi_{\tau,l}$  and  $\xi_{\tau,l}^{(0)}$  share the same non-zero  $\text{sgn}(\xi^i)$ , Eqs. (18) and (20) indicate that  $\tau l$  serves as the valley index and  $\eta \simeq i\tau l \sqrt{3}/2$ . In this case,  $\lambda = e^{ik_x a/2} \simeq e^{i\tau l \frac{2\pi}{3}}$ , and  $\lambda^2 = e^{ik_x a} \simeq e^{-i\tau l \frac{2\pi}{3}}$ . The  $\tau l = +$  mode correspond to  $K'$  valley where  $k_x a \simeq -2\pi/3$ , while the other  $\tau l = -$  mode corresponds to  $K$  valley where  $k_x a \simeq 2\pi/3$  [80]. Note that this relation holds only when Eq. (21) is a non-zero real number. Throughout this paper, we consider a mono-bi-mono junction with the current along the  $x$  direction; in this case, propagating states in the monolayer leads require  $|s| < |E + \varepsilon|$ . Since  $E + \varepsilon$  is close to zero,  $\omega$  becomes close to unity. Therefore, when the displacement is also small, Eqs. (8) and (9) reduce to approximately  $\gamma_3^{(0)}\xi$  and  $\gamma_4^{(0)}\xi$ , respectively. Although  $\gamma_3$  and  $\gamma_4$  have magnitudes comparable to  $\gamma_1$ , the smallness of  $\xi$  allows us to treat  $f_3$  and  $f_4$  as perturbations.

Neglecting the second and higher-order terms in  $f_3$  and  $f_4$ , the function  $X$  can be approximated as

$$X = \prod_{\tau=\pm} \prod_{l=\pm} \left(\xi - \xi_{\tau,l}^{(0)}\right) + \gamma_1 \left(D_\eta + \sum_{n=0}^3 D_n \xi^n\right), \quad (22)$$

where

$$D_0 = 4(c-1) \left[\bar{\gamma}_3^{(x)} - c\gamma_3^{(y)} - E(\bar{\gamma}_4^{(x)} + \gamma_4^{(y)})\right], \quad (23)$$

$$D_1 = 4(1-c)(\gamma_3^{(y)} + 2\bar{\gamma}_3^{(x)}) + 4E \left((c-2)\bar{\gamma}_4^{(x)} + c\gamma_4^{(y)}\right), \quad (24)$$

$$D_2 = (6c-4)\bar{\gamma}_3^{(x)} - 2\gamma_3^{(y)} + 4E\bar{\gamma}_4^{(x)}, \quad (25)$$

$$D_3 = -2c\bar{\gamma}_3^{(x)}, \quad (26)$$

and

$$D_\eta = 2is\eta \left[(\xi^2 - 2\xi)\hat{\gamma}_3 + 2E\hat{\gamma}_4\right]. \quad (27)$$

Owing to the approximation  $\eta \simeq i\tau l \sqrt{3}/2$ , which is justified in the second paragraph of this section, the equation  $X = 0$  can be approximately regarded as a quartic equation in  $\xi$ , even when  $\delta_x k_y \neq 0$ . This allows us to adapt the Durand-Kerner method [81, 82] to obtain the shift  $\tilde{\Delta}\xi \equiv \xi - \xi^{(0)}$  caused by the skew hopping, yielding

$$\begin{aligned} \tilde{\Delta}\xi_{\tau,l} &= \frac{-X}{\left(\xi - \xi_{-\tau,l}^{(0)}\right) \left(\xi - \xi_{\tau,-l}^{(0)}\right) \left(\xi - \xi_{-\tau,-l}^{(0)}\right)} \Bigg|_{\xi=\xi_{\tau,l}^{(0)}} \\ &= \frac{-\gamma_1 D_\eta - \gamma_1 \sum_{n=0}^3 D_n \xi^n}{-4ilq\tau \sqrt{p - s^2 + ilq}} \Bigg|_{\xi=\xi_{\tau,l}^{(0)}}. \end{aligned} \quad (28)$$

The change caused by  $\vec{\delta}$  is represented by

$$\Delta\xi_{\tau,l} \equiv \tilde{\Delta}\xi_{\tau,l} \Big|_{\vec{\delta} \neq 0} - \tilde{\Delta}\xi_{\tau,l} \Big|_{\vec{\delta} = 0}. \quad (30)$$

We refer to Eq. (29) as  $\tilde{\Delta}\xi$  approximation.

#### IV. DISPERSION LINES

Figure 3 shows the exact dispersion lines (DLs), representing the relation between  $(k_x^r a, -k_x^i a)$  and the energy  $E$ , for  $\varepsilon = 0.35$  eV,  $k_y = 0$ , and  $\vec{\delta} = 0$ . They are obtained by numerical diagonalization of the transfer matrix, as described in the Appendix B. Each DL is labeled by the index  $(\tau, l)$ . When  $k_x^i \neq 0$ , only the indices  $(\tau, l)$  corresponding to  $|\lambda| < 1$  are indicated. Here, the relation  $-k_x^i a = 2 \log|\lambda|$  holds. In the gap region,

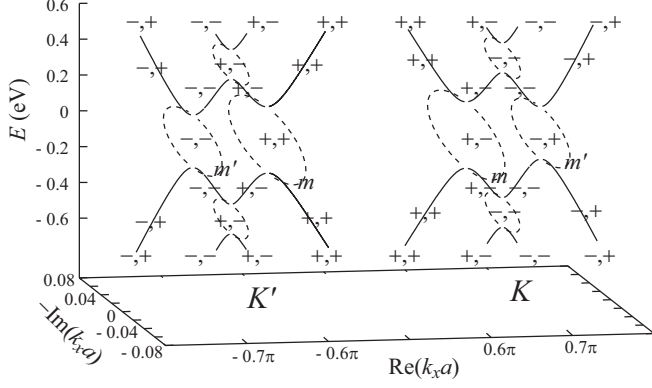


FIG. 3. The relation between  $(k_x^r a, -k_x^i a)$  and the energy  $E$  for  $\varepsilon = 0.35$  eV,  $k_y = 0$ , and  $\vec{\delta} = 0$ . Here,  $k_x^r = \text{Re}(k_x)$  and  $k_x^i = \text{Im}(k_x)$ . Each DL is labeled by  $(\tau, l)$ ; for  $k_x^i \neq 0$ , the labels are shown only for those with  $|\lambda| = \exp(-k_x^i a/2) < 1$ . See the text for the definition of  $(\tau, l)$ ,  $m$  and  $m'$ .

no RDLs exist, whereas CDLs remain. CDLs connect local extrema (minima and maxima) belonging to different RDLs. Among the zero-energy points of the CDLs in the gap, we denote by  $m$  the point satisfying  $|k_x^r a| < 2\pi/3$ , and by  $m'$  the point satisfying  $|k_x^r a| > 2\pi/3$ . The CDLs passing through these points are referred to as the  $m$ DL and  $m'$ DL, respectively. When  $\gamma_3 = \gamma_4 = 0$ , the  $m$ DL and  $m'$ DL connect to an RDL at a common energy. However, skew hopping shifts the connection energies of the  $m$ DL and  $m'$ DL relative to each other. To emphasize this shift, we choose a relatively large value (0.35 eV) of  $\varepsilon$  in Fig. 1. In the following, we instead use  $\varepsilon = 0.15$  eV. This  $\varepsilon$  is close to  $\gamma_1/2$ , corresponding to the experimentally relevant gap [11–14]. For variations induced by  $\vec{\delta}$ , the role of skew hopping becomes more significant than that of  $\gamma_1$ . This is because the change in skew hopping due to the displacement  $\vec{\delta}$  appears only at second order in  $|\vec{\delta}|$  in Eq. (1), whereas it enters linearly in  $\delta_x$  and  $\delta_y$  in Eqs. (2) and (3).

Figure 4 shows the DLs in the  $K$  valley for  $\vec{\delta} = 0$  at (a)  $k_y = 0$ , (b)  $3k_y b = 0.03\pi$ , and (c)  $3k_y b = 0.032\pi$ . The solid lines represent exact results, as in Fig. 3. The circles show results obtained within the  $\tilde{\Delta}\xi$  approximation, evaluated at  $E = -0.5, -0.48, \dots, 0.5$  eV with an energy spacing of 0.02 eV. The RDLs are labeled in ascending order of energy as  $E_1, E_2, E_3$ , and  $E_4$ . For the extrema of  $E_2$  and  $E_3$ , those connected to the  $m$ DL are labeled 2 and 3, those connected to the  $m'$ DL are labeled 2' and 3', and those connected to  $E_1$  or  $E_4$  are labeled 2'' and 3''. As  $k_y$  increases, 3' and 2' approach 3'' and 2'', respectively, and they eventually merge and disappear. In case (b), 3' and 3'' vanish, and the corresponding CDLs become detached from  $E_3$ . As a result, two CDLs merge and the  $m'$ DL connects to  $E_4$ . With further increase of  $k_y$ , 2' and 2'' also disappear, and a CDL connecting  $E_1$  and  $E_4$  emerges. The CDL generated by the merger re-

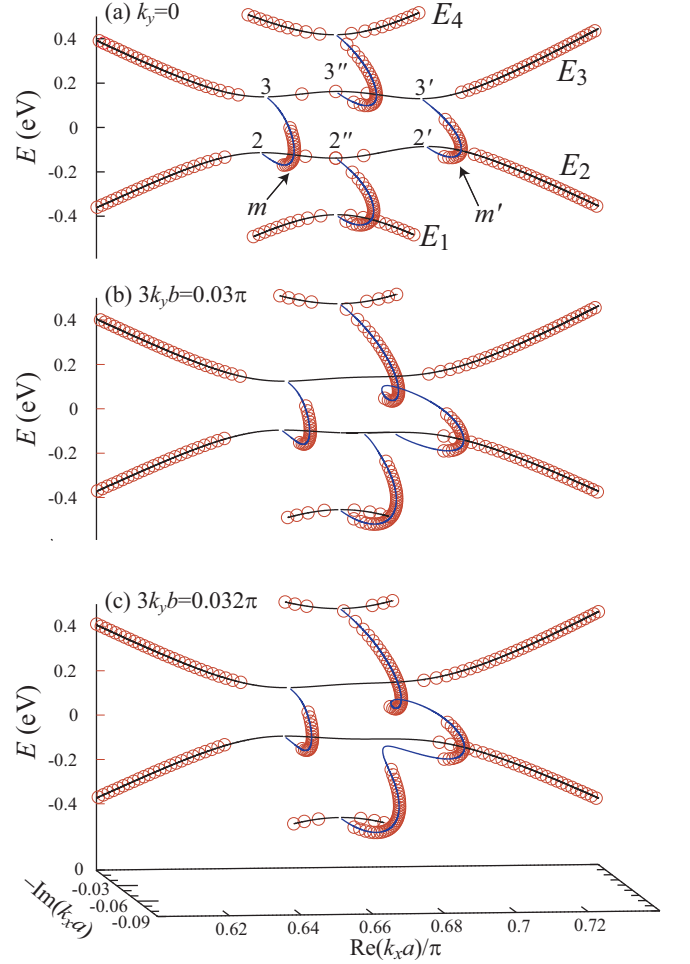


FIG. 4. The DLs in the  $K$  valley for  $\vec{\delta} = 0$  at (a)  $k_y = 0$ , (b)  $3k_y b = 0.03\pi$ , and (c)  $3k_y b = 0.032\pi$ , for  $\varepsilon = 0.15$  eV. Solid lines represent exact results, while circles correspond to the  $\tilde{\Delta}\xi$  approximation. For the circles, calculations are performed at  $E = -0.5, -0.48, \dots, 0.5$  eV with an energy spacing of 0.02 eV, except in the region where  $|q|^2 < \gamma_0^4 \times 10^{-5}$ . The RDLs are labeled in ascending order of energy as  $E_1, E_2, E_3$ , and  $E_4$ . See the text for the definitions of the points  $m, m', 2, 2', 2'', 3, 3',$  and  $3''$ .

tains a memory of its original shape and subsequently drifts. As is clear from the analytical expressions, when  $q$  is close to zero, *i.e.*, near the gap edge of the  $\gamma_1$ -only tight-binding model, the  $\tilde{\Delta}\xi$  approximation diverges and becomes invalid. Accordingly, circles are not shown when  $|q|^2 < \gamma_0^4 \times 10^{-5}$ . Away from this region, the  $\tilde{\Delta}\xi$  approximation reproduces both CDLs and RDLs and accurately describes the exact DLs.

The top, middle, and bottom panels of Fig. 5 show the CDLs for  $\vec{\delta} = (0, 0)$ ,  $(0, 1)$ , pm, and  $(0, -1)$ , pm in the  $K$  valley. The top and bottom panels of Fig. 6 show the CDLs for  $\vec{\delta} = (1, 0)$ , pm in the  $K$  and  $K'$  valleys, respectively. The left (right) panels indicate the projections onto the  $(|k_x^r| a, -k_x^i a)$  [ $(E, -k_x^i a)$ ] plane. Calcula-

lations within the  $\tilde{\Delta}\xi$  approximation are performed at  $E = -0.3, -0.29, \dots, 0.3$  eV with an energy spacing of 0.01 eV, and the circles represent these data. The lines represent the exact results, as in Fig. 4. As in Fig. 4, the approximate results are not shown when  $|q|^2 < \gamma_0^4 \times 10^{-5}$ . We choose three values of  $3k_y b$ : 0,  $0.02\pi$ , and  $0.04\pi$ . In the same way as Fig. 4 (c), the merged CDLs drift at  $3k_y b = 0.04\pi$ . Comparing the middle and bottom panels with the top panels at the  $m$  and  $m'$  points in Fig. 5, one observes clear  $\delta_y$  effects at zero energy. A positive  $\delta_y$  shifts  $|\lambda|$  toward unity, suggesting an enhancement of the conductance  $G$  of the mono-bi-mono junction. Conversely, a negative  $\delta_y$  drives  $|\lambda|$  away from unity and is expected to reduce  $G$ . In Fig. 4(b), the positive-energy extrema  $3'$  and  $3''$  disappear, whereas the negative-energy extrema  $2'$  and  $2''$  at  $E_2$  remain, indicating an energy asymmetry induced by  $\gamma_4$ . However, in Figs. 5 and 6, the spectra around the  $m$  and  $m'$  points are nearly symmetric with respect to energy, suggesting that the effects of  $\gamma_4$  are weak. This is consistent with Eq. (29), in which the  $\gamma_4$  terms are always multiplied by  $E$ , which is close to zero. Comparing Fig. 6 with the top panel of Fig. 5, one finds that the effect of  $\delta_x$  almost vanishes at  $k_y = 0$ . Within the  $\tilde{\Delta}\xi$  approximation, the dominant contribution of  $\delta_x$  arises through  $D_\eta$ , which is exactly zero at  $k_y = 0$ . For  $3k_y b/2 = 0.04\pi$ , the formation of drifting CDLs becomes valley asymmetric. In the  $K'$  valley, the  $m'$ DL undergoes merging and drifting, as in the case  $\delta_x = 0$ . In contrast, in the  $K$  valley, the  $m$ DL exhibits drifting behavior.

Table I lists the values of  $(|k_x^r|a/\pi - 0.66, -k_x^i a) \times 10^4$  at the  $m$  and  $m'$  points, evaluated within the  $\Delta\xi$  approximation, while Table II summarizes the corresponding changes induced by the displacement  $\vec{\delta}$ . The effect of  $\delta_x$  on  $|\lambda|$  has opposite signs at  $m$  and  $m'$  and tends to cancel out. Since the sign of  $\delta_x s$  is fixed in Fig. 6, this cancellation is not due to a sign reversal of  $\delta_x s$ . In addition to inter-valley compensation, the cancellation also occurs within a single valley. From this cancellation, we expect that the effect of  $\delta_x$  on the conductance  $G$  of a mono-bi-mono junction is weaker than that of  $\delta_y$ .

To provide a physical interpretation of Table II, we further simplify Eq. (29) under the following conditions. (i) As mentioned above Eq. (22), we consider only values of  $s$  close to zero. (ii) Since  $E$  is close to zero, the term  $\gamma_4$  is neglected. (iii) Because  $\tilde{\gamma}_3^{(x)}$  is insensitive to the shear displacement  $\vec{\delta}$ , we neglect  $D_3$ . Condition (i) follows  $-\tau\sqrt{p-s^2+ilq} \simeq \xi_{\tau,l}^{(0)}$ . Under these conditions, we obtain

$$\Delta\xi_{\tau,l} \simeq i\frac{\sqrt{3}\gamma_1}{2q}s\tau\hat{\gamma}_3 - il\theta\xi_{\tau,l}^{(0)}, \quad (31)$$

where

$$\theta \equiv \frac{\gamma_1}{2|q|}\left(\gamma_3^{(y)} - \gamma_3^{(0)}\right). \quad (32)$$

Though we take  $q$  as a positive real number in this section,  $|q|$  is used in Eq. (32) to accommodate the later

case where  $q$  becomes purely imaginary. Here, using  $c-1 \simeq -s^2/2$ , we neglect the terms  $D_0$  and  $D_1$ , which are of second order in  $s$ , while retaining  $D_\eta$ , which is linear in  $s$ . Furthermore, since  $|\xi| \ll 1$ , only terms linear in  $\xi$  are retained in Eq. (27). From Eq. (31), we derive

$$\Delta|\xi_{\tau,l}^i| = -\frac{\sqrt{3}\gamma_1}{2q}s\tau\hat{\gamma}_3 - \theta\left|\text{Re}(\xi_{\tau,l}^{(0)})\right|, \quad (33)$$

and

$$\Delta|\xi_{\tau,l}^r| = \theta\left|\text{Im}(\xi_{\tau,l}^{(0)})\right| \quad (34)$$

Assuming that the perturbation  $f_3$  does not alter the signs of real and imaginary parts of  $\xi_{\tau,l}$ , we use relations  $|\xi^i| = \text{sgn}(\xi^i)\xi^i = -\tau l\xi^i$  and  $|\xi^r| = \text{sgn}(\xi^r)\xi^r = -\tau\xi^r$ . Since  $\hat{\gamma}_3$  and  $\theta$  respond negatively to  $\delta_x$  and positively to  $\delta_y$ , respectively, and since  $|\xi^r/\sqrt{3}| \simeq |k_x^r a \mp (2\pi/3)|$ , Eqs. (33) and (34) are consistent with Table II. As shown in Fig. 3, the  $m$  and  $m'$  points correspond to  $l = -$  and  $l = +$  in the  $K$  valley, and to  $l = +$  and  $l = -$  in the  $K'$  valley, respectively. It should be emphasized that Eq. (31) is introduced solely for the purpose of providing a physical interpretation of the results. All numerical results within the  $\tilde{\Delta}\xi$  approximation are obtained directly from the original Eq. (29).

## V. CONDUCTANCE OF MONO-BI-MONO JUNCTIONS

We consider a mono(+)-bi( $\mp$ )-mono(+) junction, in which the thickness of the energy barrier is determined by the length of the  $-$  layer, given by  $(N-2)a/2$ . The definition of  $N$  follows that adopted in Ref. 1, and Fig. 1 (a) corresponds to the case  $N = 6$ . In accordance with the Bloch factors discussed in the preceding section, the transport direction is taken along the  $x$  axis, and the interfaces between the monolayer and bilayer regions are assumed to be ideal armchair boundaries. Figure 7 shows the zero-energy conductance  $G$  of a mono-bi-mono junction calculated using the Landauer formula and plotted as a function of  $N$  in units of  $G_0 = 2e^2/h$  [1, 2, 83]. In the exact numerical calculation shown in panel (a), the Bloch factor  $\Lambda = \exp(ik_x a)$ , corresponding to the translation vector  $(a, 0)$ , is employed. This  $\Lambda$  is obtained exactly by numerically diagonalizing the transfer matrix. Panels (b) and (c) show the results obtained by replacing  $\Lambda$  in the same numerical code with  $\lambda^2$  and  $\lambda^2/|\lambda|^2$ , respectively. Here,  $\lambda$  represents the approximate quantity  $\exp(ik_x a/2)$  obtained from Eq. (29). The details of the calculation are provided in the Appendix B [84].

We impose periodic boundary conditions in the  $y$  direction with a width of  $3000b$ , which yields a discretization interval of  $\pi/(1500b)$  for  $k_y$ . Only the  $k_y$  modes for which the wave numbers in the monolayer leads on both sides are real contribute to the conductance. The contributing range is approximately given by  $|3k_y b| < |2\varepsilon/\gamma_0| \simeq 0.1$ . Therefore, among the data shown in Figs. 5 and 6, the

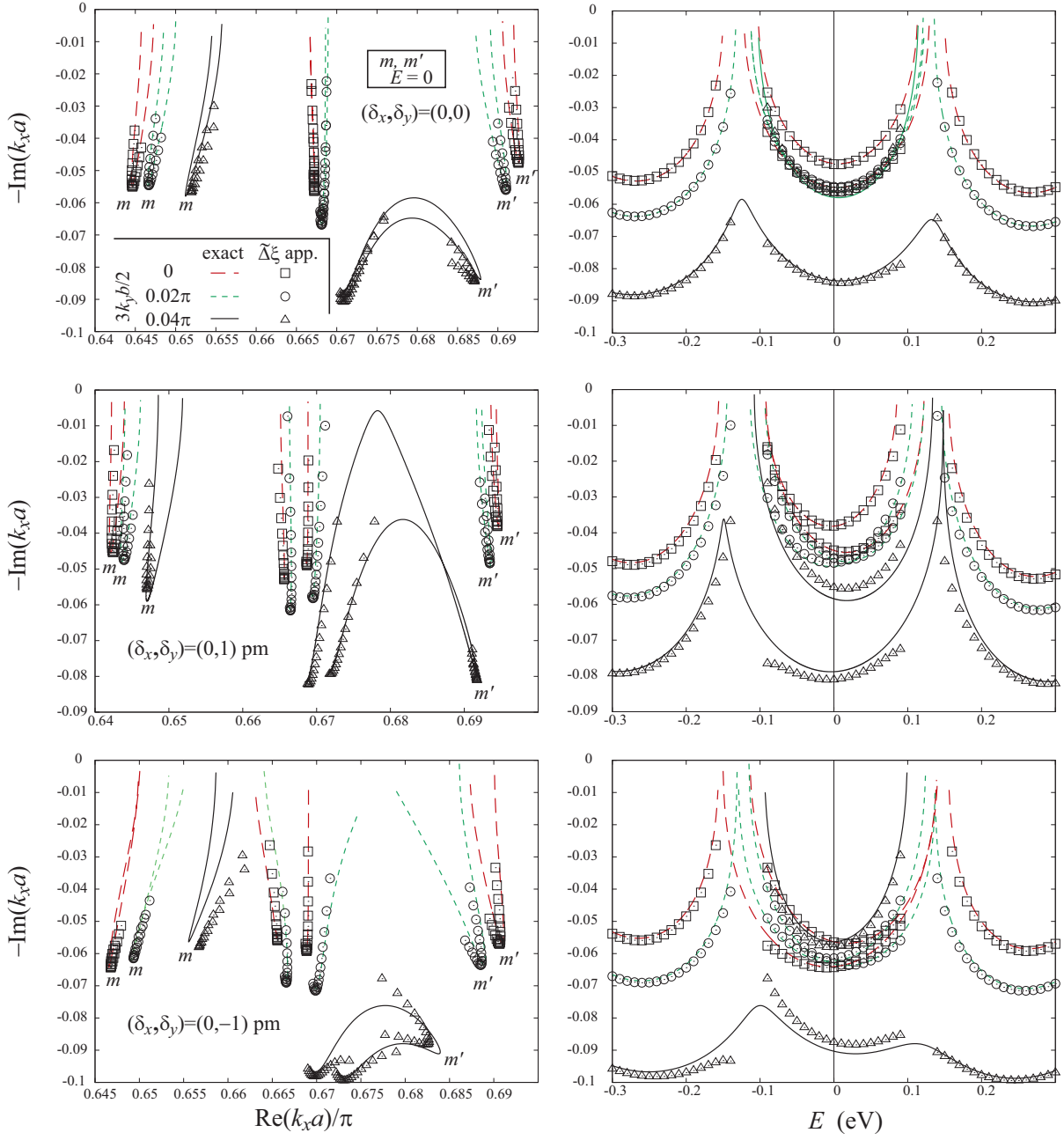


FIG. 5. CDLs in the  $K$  valley for  $\varepsilon = 0.15$  eV and three values of  $3k_y b/2$ . The top, middle, and bottom panels correspond to  $\vec{\delta} = (0, 0)$ ,  $(0, 1)$  pm, and  $(0, -1)$  pm, respectively. Solid, dotted, and dashed lines represent exact results, whereas squares, circles, and triangles denote results obtained within the  $\tilde{\Delta}\xi$  approximation. The approximation results are evaluated at  $E = -0.3, -0.29, \dots, 0.3$  eV with an energy spacing of 0.01 eV, except in the region where  $|q|^2 < \gamma_0^4 \times 10^{-5}$ . Different line styles and symbols correspond to different values of  $k_y$ , as indicated in the legend. The left and right panels show projections onto the  $(k_x^i a/\pi, -k_x^i a)$  and  $(E, -k_x^i a)$  planes, respectively. Vertical lines at  $E = 0$  in the right panels indicate the correspondence with the points  $m$  and  $m'$  in the left panels.

$m$  and  $m'$  points at  $k_y = 0$  have the largest impact on Fig. 7. The number of allowable  $k_y$  modes is 31 in each valley, resulting in a total of 62 transport channels. For  $N < 10$ , the barrier becomes extremely thin, and the conductance  $G$  approaches its maximum value

$62G_0$ . Open squares, circles, triangles, and filled squares represent the cases  $\vec{\delta} = (0, 0)$ ,  $(0, 1)$  pm,  $(0, -1)$  pm and  $(1, 0)$  pm, respectively. Because period-3 oscillations originating from  $k_x^i a \simeq \pm 2\pi/3$  appear, the data are classified according to the remainder  $\text{mod}(N)$  upon division

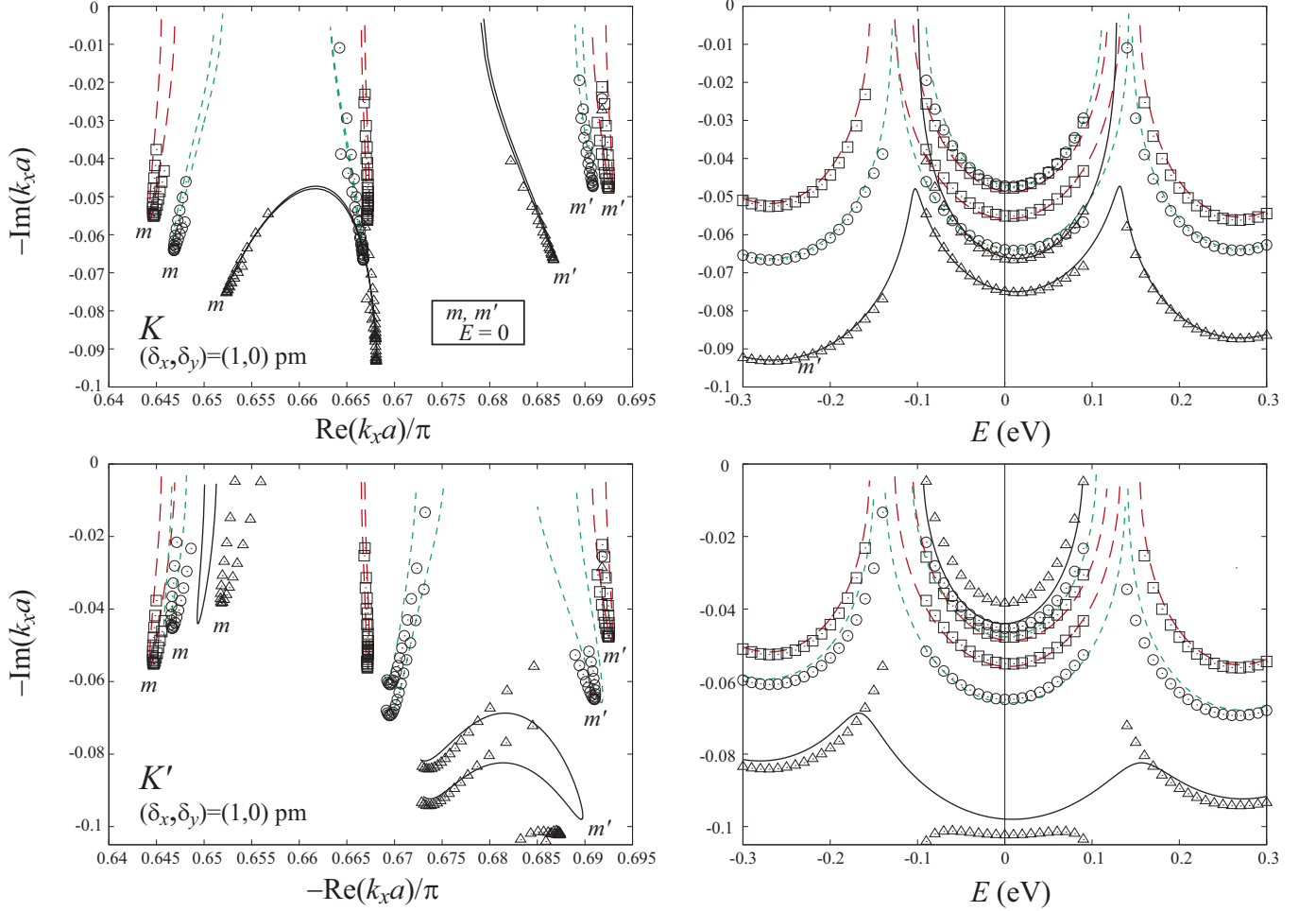


FIG. 6. CDLs for  $\varepsilon = 0.15$  eV and  $\vec{\delta} = (1, 0)$  pm. The top and bottom panels correspond to the  $K$  and  $K'$  valleys, respectively. The projections in the left and right panels and the legend are the same as in Fig. 4. In the bottom left panel,  $|k_x^r|a/\pi$  is used as the horizontal axis.

TABLE I. Complex wave numbers  $k_x$  at  $E = 0$  for different shear displacements  $\vec{\delta} = (\delta_x, \delta_y)$  pm, including the case  $\vec{\delta} = 0$ , evaluated within the  $\Delta\xi$  approximation and shown in the format  $(|k_x^r|a/\pi - 0.66, -k_x^i a) \times 10^4$ , corresponding to Figs. 5 and 6. See the text for the definitions of  $m$  and  $m'$ .

$(\delta_x, \delta_y)$ valley	$k_y = 0$		$3k_y b = 0.02\pi$		$3k_y b = 0.04\pi$	
	$m$	$m'$	$m$	$m'$	$m$	$m'$
(0, 0) $K$	(-154, -550)	(326, -476)	(-134, -544)	(310, -560)	(-81, -568)	(271, -844)
(0, 1) $K$	(-177, -449)	(345, -380)	(-162, -471)	(335, -484)	(-130, -552)	(317, -811)
(0, -1) $K$	(-132, -642)	(307, -565)	(-107, -615)	(286, -630)	(-33, -581)	(227, -875)
(1, 0) $K$	(-153, -551)	(325, -477)	(-132, -639)	(308, -472)	(-76, -750)	(267, -665)
(1, 0) $K'$	(-153, -551)	(325, -477)	(-134, -453)	(310, -649)	(-82, -384)	(273, -1024)

by 3. For  $\text{mod}(N) = 2$  and  $\text{mod}(N) = 0$ , the data are vertically shifted by  $20G_0$  and  $40G_0$ , respectively. The displacement-induced change in the conductance,  $\Delta G$ , can be identified from the difference relative to the open square symbols. The close agreement between panels (a) and (b) demonstrates that both  $G$  and  $\Delta G$  are well described by the  $\lambda$  obtained from Eq. (29). Relation between  $\Delta G$  and  $\vec{\delta}$  agrees with  $\Delta k_x^i$  in Table II for the data

with  $N > 60$ . Specifically, for  $\vec{\delta} = (0, \pm 1)$  pm, the signs of  $\delta_y$ ,  $\Delta|\lambda|$ , and  $\Delta G$  are consistent, whereas  $\Delta G$  is relatively small for  $\vec{\delta} = (1, 0)$  pm. However, for  $N < 50$ , the relation between  $\Delta G$  and  $\delta_y$  tends to be opposite to that observed for larger  $N$ . This sign reversal is reproduced in Fig. 7(c). When  $N$  is small,  $|\lambda|^N$  remains close to unity, and the oscillatory effect originating from the phase of  $\lambda$  dominates over the attenuation effect. When

TABLE II. Changes in the complex wave numbers  $k_x$  at  $E = 0$  induced by the shear displacement  $\vec{\delta}$ , evaluated within the  $\Delta\xi$  approximation and shown in the same format as in Table I. The values represent  $k_x(\vec{\delta} \neq 0) - k_x(\vec{\delta} = 0)$ .

$(\delta_x, \delta_y)$ , valley	$k_y = 0$		$3k_y b = 0.02\pi$		$3k_y b = 0.04\pi$	
	$m$	$m'$	$m$	$m'$	$m$	$m'$
$(0, 1) K$	$(-23, 100)$	$(19, 95)$	$(-28, 73)$	$(24, 76)$	$(-50, 15)$	$(46, 34)$
$(0, -1) K$	$(22, -93)$	$(-19, -89)$	$(27, -71)$	$(-24, -70)$	$(48, -13)$	$(-45, -31)$
$(1, 0) K$	$(1, -1)$	$(-1, -1)$	$(2, -96)$	$(-2, 88)$	$(4, -182)$	$(-5, 180)$
$(1, 0) K'$	$(1, -1)$	$(-1, -1)$	$(0, 91)$	$(0, -89)$	$(-1, 183)$	$(2, -179)$

$70 < N < 80$  and  $\delta_x = 0$ , on the other hand, Figs. 7(b) and 7(c) exhibit the same sign of  $\Delta G/\delta_y$ , indicating that the effects of the real and imaginary parts of the longitudinal wave number,  $k_x^r$  and  $k_x^i$ , reinforce each other. As shown in Table II, an increase in  $\delta_y$  leads to an increase in  $|2\xi^r| \simeq \sqrt{3}|k_x^r a \mp 2\pi/3|$ , resulting in a shorter oscillation period of the conductance  $G$  as a function of  $N$ .

Although the armchair edge is known to be the most stable graphene edge structure, the monolayer-bilayer interfaces realized in experiments may deviate from an ideal armchair configuration. For example, defects in which carbon dimers partially attach to the interface would locally increase the effective value of  $N$ . However, as shown in the figures, the characteristic positive response of the conductance  $G$  to  $\delta_y$  becomes essentially independent of  $\text{mod}(N)$  in the regime where the effects of  $k_x^r$  and  $k_x^i$  reinforce each other. Therefore, the influence of such local defects on the conductance is expected to be minor within the parameter range considered here. In realistic systems, the transverse width  $3N_y b$  is finite, which inevitably leads to the formation of edges parallel to the  $x$  axis, such as zigzag edges. These edges can host edge bands inside the gap. Since the number of such edge bands is of order unity and does not scale with  $N_y$ , their contribution to the conductance is expected to be on the order of  $G_0$ . In contrast, the contribution to  $G$  from the evanescent states considered in the present work scales linearly with  $N_y$ . For sufficiently large  $N_y$ , this contribution therefore dominates over that from the edge bands. Indeed, for the value of  $N_y = 1000$  used in Fig. 7, the change in conductance  $\Delta G$  already exceeds  $G_0$ .

## VI. $\tilde{\Delta}E$ APPROXIMATION

In the perturbative calculation presented in this section, the quantity  $\lambda$  obtained from Eqs. (16) and (20), together with the corresponding wave function

$$\vec{\psi}_{\tau,l} = \begin{pmatrix} \frac{(E+\varepsilon)\omega}{\tau\sqrt{p+ilq-s^2-is}} \\ 1 \\ \rho_{\tau,l}\beta_l \frac{(E-\varepsilon)\omega^*}{\tau\sqrt{p+ilq-s^2+is}} \\ \rho_{\tau,l}\beta_l \end{pmatrix}, \quad (35)$$

constitutes the unperturbed state, where

$$\rho_{\tau,l} = \omega^2 \frac{\tau\sqrt{p-s^2+ilq+is}}{\tau\sqrt{p-s^2+ilq-is}}, \quad (36)$$

and

$$\beta_l = \frac{2\varepsilon E - ilq}{\gamma_1(E - \varepsilon)}. \quad (37)$$

We define the perturbation  $H_{\gamma_3}$  by retaining only the  $f_3^{(\pm)}$  terms in Eq. (5) and setting all other terms to zero. As discussed in the preceding section, the effect of  $\gamma_4$  can be neglected in the vicinity of  $E = 0$ . Therefore, we set  $\gamma_4 = 0$  in  $H_{\gamma_3}$ . The energy shift induced by  $H_{\gamma_3}$  is then given, within first-order perturbation theory, by

$$\tilde{\Delta}E_{\tau,l} = \frac{{}^t\vec{\psi}_{\tau,l}^* H_{\gamma_3} \vec{\psi}_{\tau,l}}{|\vec{\psi}_{\tau,l}|^2}. \quad (38)$$

We refer to this approximation as the  $\tilde{\Delta}E$  approximation. The RDL is obtained through the following procedures. (i) The value  $\xi^{(0)}$  at  $E = E'$  is calculated from Eq. (20). Using the relation  $\xi^{(0)} - 1 = 2\cos(k_x a/2)$ , we obtain the RDL data  $(k_x a, E')$  for the only- $\gamma_1$  model. (ii) Substituting  $E = E'$  into Eq. (38), we obtain the RDL data  $(k_x a, E' + \tilde{\Delta}E_{\tau,l})$  for the  $\tilde{\Delta}E$  approximation. The data set of  $E'$  are common in procedures (i) and (ii), and  $q$  is restricted to be purely imaginary in Eq. (21), so that  $iq = |q|$ . For the RDL, both  $k_x$  and  $E$  are real quantities. Consequently, one may either fix  $E$  and evaluate the change in  $\xi$  within the  $\tilde{\Delta}\xi$  approximation, or fix  $k_x$  and evaluate the energy shift within the  $\tilde{\Delta}E$  approximation. For the CDL, however,  $k_x$  generally has both real and imaginary parts, and it is not possible to fix them simultaneously. As a result, the  $\tilde{\Delta}E$  approximation, which requires  $k_x$  to be fixed at a real value, cannot be applied to the CDL. In the CDL,  $q$  is real and  $H_{\gamma_3}$  is non-Hermitian; consequently, Eq. (38) becomes complex. The  $\tilde{\Delta}\xi$  approximation is applicable to both the RDL and the CDL, but it breaks down near the band edge of the gap, where  $q \rightarrow 0$ . In contrast, although the  $\tilde{\Delta}E$  approximation is restricted to the RDL, it remains valid even at the gap edge and is therefore complementary to the  $\tilde{\Delta}\xi$  approximation.

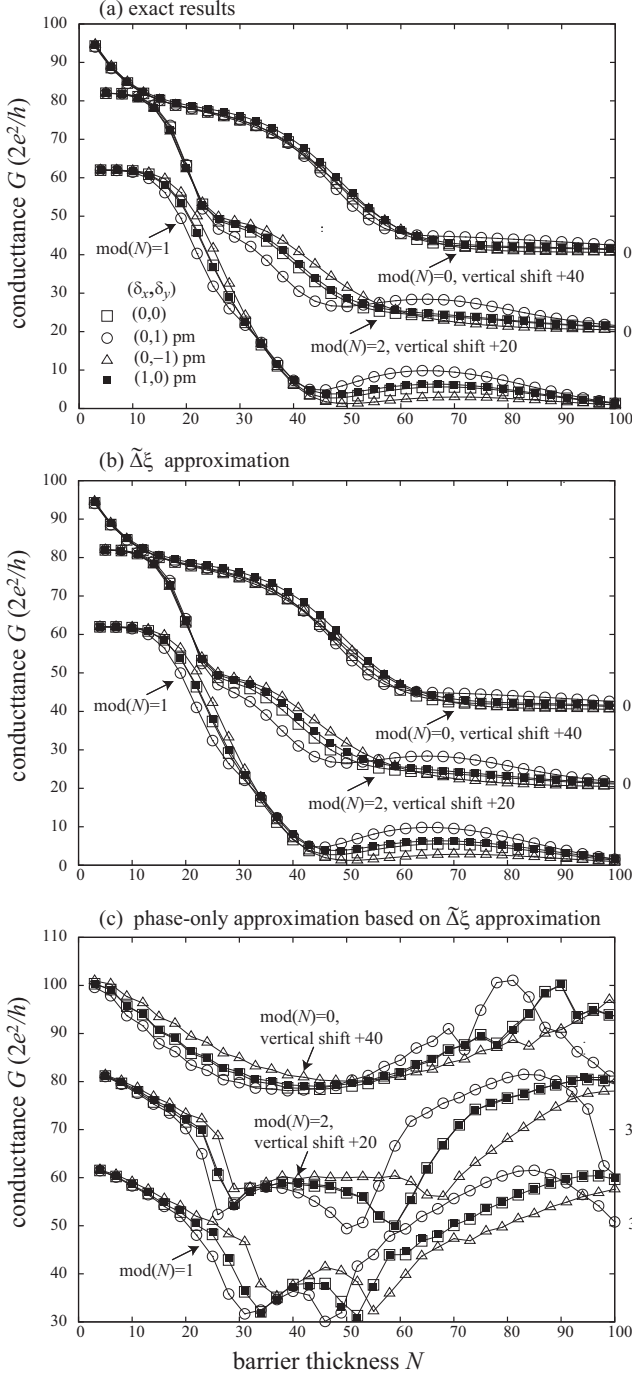


FIG. 7. The zero-energy conductance  $G$  of mono-bi-mono junctions, calculated from the Landauer formula with periodic boundary conditions in the  $y$  direction assuming a transverse width of  $3000b$ , for  $\varepsilon = 0.15$  eV. For  $\text{mod}(N) = 2$  and  $\text{mod}(N) = 0$ , the data are vertically shifted by 20 and 40, respectively, in units of  $G_0 = 2e^2/h$ . See the text for the definition of  $\text{mod}(N)$ .

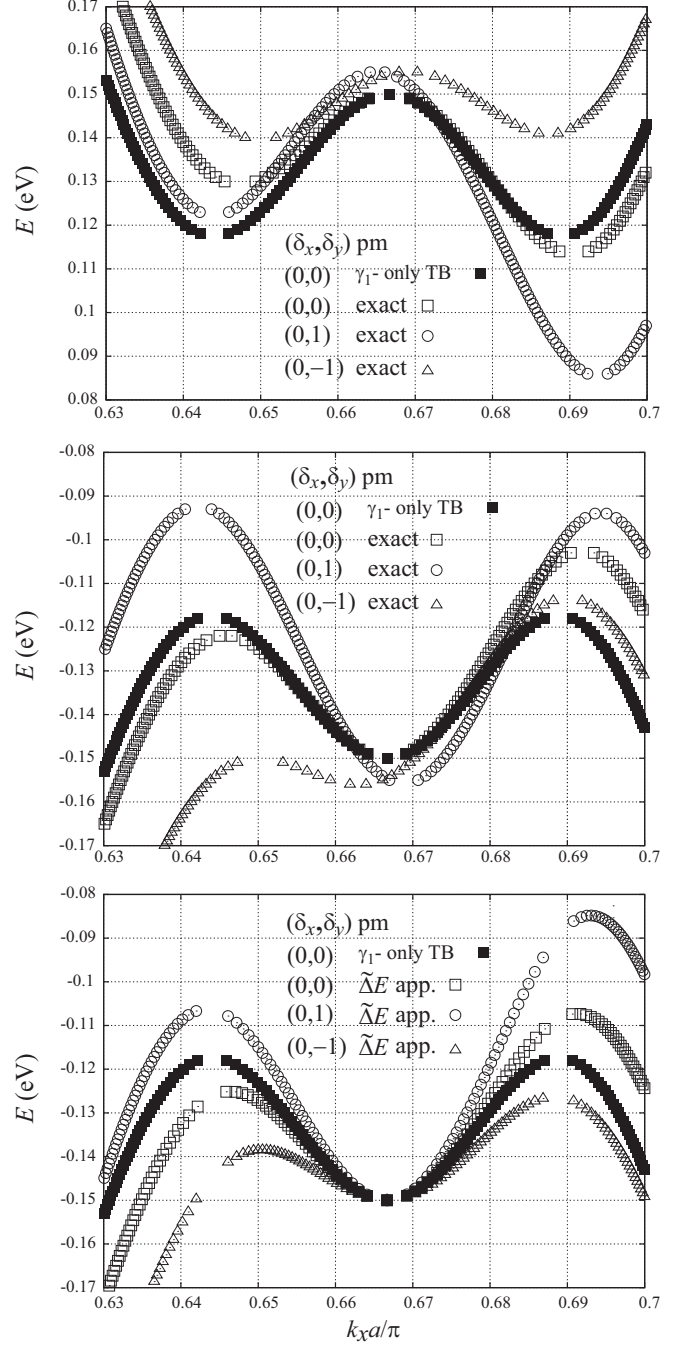


FIG. 8. The RDL for  $k_y = 0$  and  $\varepsilon = 0.15$  eV. Except for the filled square symbols, the top, middle, and bottom panels show the exact  $E_3$ , the exact  $E_2$ , and the values of  $E' + \tilde{\Delta}E_{\tau,l}$  corresponding to  $E_2$ , respectively. The approximate results are evaluated with an  $E'$  spacing of 0.001 eV. The exact RDL is calculated as a function of  $E$  with an energy spacing of 0.001 eV. See the text for the definition of  $E'$ .

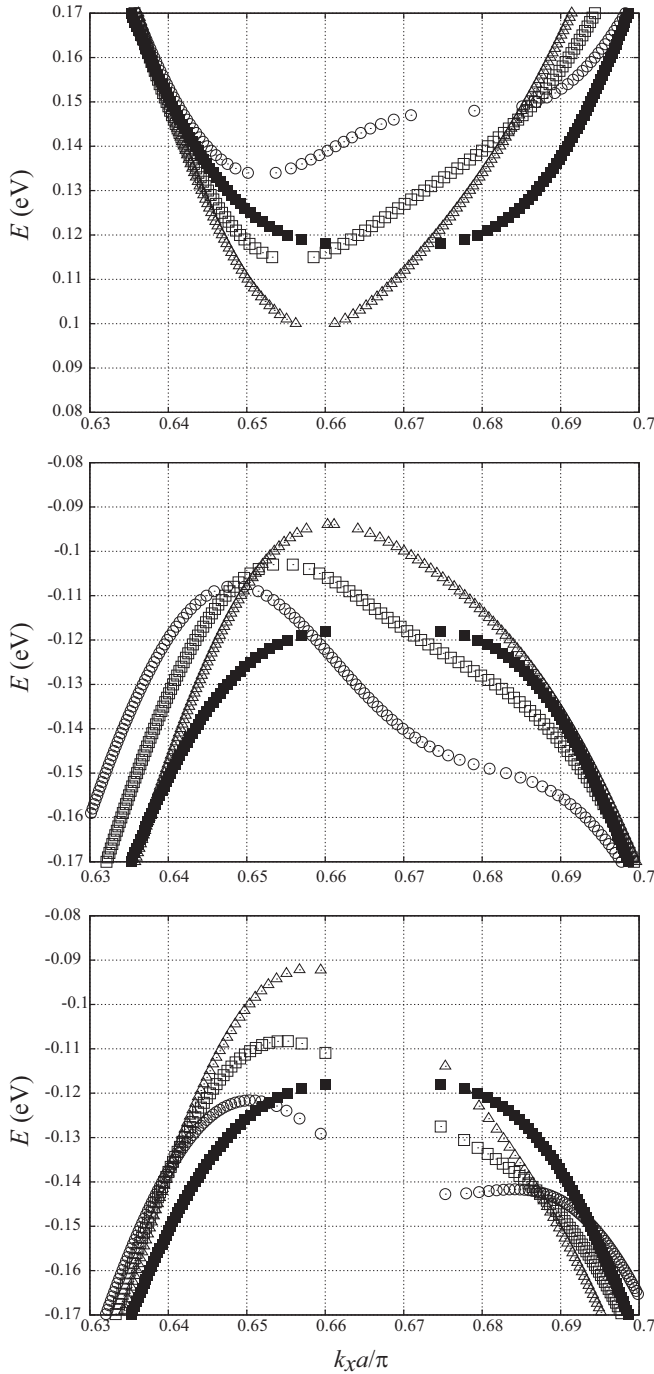


FIG. 9. The RDL for  $3k_y b = 0.04\pi$  and  $\varepsilon = 0.15$  eV. The panel arrangement, the  $E'$  spacing used for the approximate results, the energy spacing used for the exact calculations, and the legend are the same as those in Fig. 8.

From the results of the previous section, the effect of  $\delta_x$  was found to be small; we therefore focus on the case  $\delta_x = 0$ . Figure 8 shows the RDL for  $k_y = 0$ , while Fig. 9 shows the RDL for  $3k_y b = 0.04\pi$ . Filled square symbols represent the RDL data ( $k_x a, E'$ ). All other symbols correspond to the RDL in the presence of skew

interlayer hopping: open squares, circles, and triangles represent  $\delta_y = 0, 1$  pm, and  $-1$  pm, respectively. Except for the filled square symbols, the top, middle, and bottom panels depict the exact  $E_3$ , the exact  $E_2$ , and the approximate values  $E' + \tilde{\Delta}E_{\tau,l}$  corresponding to  $E_2$ . Square symbols correspond to  $\gamma_1 = \gamma_1^{(0)}$ , whereas non-square symbols correspond to  $\gamma_1 \neq \gamma_1^{(0)}$ . However, the  $k_x a$  data set obtained in procedure (i) hardly depends on  $\delta_y$ . This dependence is extremely small but still barely visible around  $k_x a = 0.66\pi$  in the bottom panel of Fig. 9. The exact values of  $k_x a$  are obtained from the eigenvalues of the transfer matrix, as explained in Appendix B. For a consistent comparison, the exact calculations are carried out as a function of  $E$  using the same numerical grid as that adopted for  $E'$  in the  $\tilde{\Delta}E$  approximation. Within the  $\tilde{\Delta}E$  approximation,  $E_3(k_x) = -E_2(k_x)$ , and we therefore omit the presentation of the positive-energy branch. Although the filled square symbols are also symmetric with respect to energy, they are retained in the top panel in order to illustrate the effect of skew interlayer hopping in the absence of shear displacement. In the exact numerical calculations, on the other hand,  $\gamma_4$  is retained in the Hamiltonian, leading to an energy asymmetry. Since the calculations in procedure (i) are performed as a function of  $E'$  with a spacing of 0.001 eV, the filled square symbols become sparse when the RDL is nearly flat. Consequently, they are absent near  $k_x a = 0.67\pi$  in Fig. 9. Because the perturbation  $H_{\xi_3}$  does not modify  $k_x$  within the  $\tilde{\Delta}E$  approximation, except for a very small  $\gamma_1 - \gamma_1^{(0)}$  effect, the same missing-data behavior is observed for the open symbols in the bottom panel of Fig. 9. The difference between the filled and open square symbols is due to the effect of skew interlayer hopping in the absence of shear displacement, i.e., the  $\gamma_{3,4}^{(0)}$  effect. In contrast, the changes in the triangular and circular symbols relative to the open squares represent the effect of  $\delta_y$ , namely the  $\gamma_{3,4} - \gamma_{3,4}^{(0)}$  effect. Although the relative ordering of the four symbols is not necessarily identical between the exact and approximate results, the  $\gamma_{3,4}^{(0)}$  and  $\gamma_{3,4} - \gamma_{3,4}^{(0)}$  effects are in good overall agreement. The experimentally observable effect is not  $\gamma_{3,4}^{(0)}$  itself, but rather the  $\gamma_{3,4} - \gamma_{3,4}^{(0)}$  contribution. The overall shape of the RDL and the magnitude of the splitting are well reproduced by the  $\tilde{\Delta}E$  approximation.

Comparing the present results with those for  $3k_y b = 0$  and  $0.04\pi$  discussed in the previous section, we find that, for Fig. 8, a natural relation holds whereby  $|\lambda|$  approaches unity as the gap width decreases. In Fig. 9, the  $\gamma - \gamma^{(0)}$  effect has a magnitude comparable to that in Fig. 8 but with the opposite sign, whereas no such sign reversal is observed in Table II. However, for most of the  $k_y$  range that contributes to the junction conductance  $G$ , the natural relation at  $k_y = 0$  is preserved. For  $k_y = 0$ ,  $\Delta E_{\tau,l} = \tilde{\Delta}E_{\tau,l}(\delta_y \neq 0) - \tilde{\Delta}E_{\tau,l}(\delta_y = 0)$  reduces to simple

forms:

$$\Delta E_{\tau,l} \simeq \frac{4|q|\beta_l\theta}{\gamma_1 \left| \psi_{\tau,l}^{(0)} \right|^2}, \quad (39)$$

The interlayer wave-function ratio  $\beta$  appearing in Eq. (39) explicitly shows, through Eq. (38), that it represents the strength of interlayer chemical bonding mediated by  $\gamma_3$ . Since  $iq = |q| \simeq 0$  and  $|E| < |\varepsilon|$ ,  $\beta$  and  $E$  have opposite signs. As  $\theta$  has positive response to  $\delta_y$ , Eq. (39) acquires the opposite sign to  $E\delta_y$ . This result is consistent with Ref. [53] and indicates that variations in the  $\gamma_3$ -induced interlayer coupling are responsible for the changes in both the band-gap width and  $|\lambda|$ .

## VII. IN-PLANE SUBLATTICE WAVE-FUNCTION RATIO

In this section, we analyze the quantity  $\circ_{\pm}/\bullet_{\pm}$ , i.e., in-plane sublattice wave-function ratio (ISWR). The ISWR, often interpreted as a sublattice pseudospin, provides a compact description of the internal phase structure [78, 79]. Although the ISWR is not directly observable, it offers valuable insight into the structure of decaying modes. Since the effects of  $\delta_x$ ,  $k_y$ , and  $\gamma_4$  were found to be small, we consider the Hamiltonian matrix  $H'$  with these parameters set to zero. We further define  $H''$  as the Hamiltonian obtained from  $H'$  by setting  $\gamma_3 = 0$ . The same notation is used for the corresponding wave functions ( $\circ_{\pm}, \bullet_{\pm}$ ) and for  $\xi$ . From the secular equation of  $H''$ , we obtain

$$\left( E \pm \varepsilon - \gamma_1 \frac{\circ''_{\pm}}{\bullet''_{\pm}} \right) \frac{\circ''_{\pm}}{\bullet''_{\pm}} = -\xi'', \quad (40)$$

where  $\xi'' = \xi^{(0)}|_{k_y=0} = -\tau\sqrt{p+ilq}$  [85]. As Eq. (35) indicates,  $\circ''_{-}/\bullet''_{+} = \beta_l(E - \varepsilon)/(E + \varepsilon)$ , we obtain

$$\frac{\circ''_{\pm}}{\bullet''_{\pm}} = -\frac{E \pm \varepsilon}{p + ilq} \xi''. \quad (41)$$

By replacing  $\circ''_{\pm}/\bullet''_{\pm}$  and  $\xi''$  in Eq. (41) with  $\circ'_{\pm}/\bullet'_{\pm}$  and  $\xi'$ , respectively, we obtain an approximate formula

$$\frac{\circ'_{\pm}}{\bullet'_{\pm}} = \tau \frac{E \pm \varepsilon}{\sqrt{p+ilq}} e^{-il\theta}, \quad (42)$$

where  $\xi' = \xi'' + \Delta\xi \simeq \xi'' \exp(-il\theta)$  has been used. Equation (42) has the following properties. (a) For fixed  $(\tau, l)$ , since  $|\varepsilon| > |E|$ , the interlayer phase difference is  $\pi$ . (b) For fixed  $l$  and a given layer, reversing the sign of  $\tau$  causes the  $\pi$  phase change. (c) For fixed  $\tau$  and a given layer, reversing the sign of  $l$  yields the complex conjugate. Because  $k_y = 0$ , the system preserves time-reversal symmetry, and property (c) holds. Equations (18) and (20) show that both operations (b) and (c) correspond to valley exchange, while operation (b) is not a complex conjugation.

Although chiral symmetry is present when  $\gamma_4 = 0$ , operation (b) does not correspond to a chiral transformation. The amplitudes ( $\circ_{+}, \circ_{-}$ ) changes into  $(-\circ_{+}, -\circ_{-})$  in operation (b), whereas it changes into  $(\circ_{+}, -\circ_{-})$  in a chiral transformation [86, 87]. This is closely related to a valley current reversal [15–17, 84, 88].

In addition to the analytical result of Eq. (42), we also obtained exact ISWRs from the eigenvectors of the transfer matrix, as shown in Appendix B. We found that the ISWR phase  $\phi$  exhibits a clearer dependence on  $\delta_y$  than the ISWR magnitude. We therefore focus our discussion on the phase  $\phi$  and omit the presentation of the magnitude. The inset of Fig. 10 shows the energy dependence of the phase  $\phi_0 \equiv \arg[\exp(-i\theta)/\sqrt{p+ilq}]$ , obtained from Eq. (42) without  $\gamma_4$ . Within this approximation, the ISWR phase  $\phi$  takes the values  $\pm\phi_0$  and  $\pi \pm \phi_0$ . The main panels show the exact  $\phi$ . In the exact calculations, the parameter  $\gamma_4$  is retained in the Hamiltonian, leading to an asymmetry in  $E$ . Squares, circles, and triangles correspond to  $\delta_y = 0, 1$  pm, and  $-1$  pm, respectively. Here, open and filled symbols correspond to the  $+$  and  $-$  layers, respectively. The vertical arrows indicate the change in the phase,  $\Delta\phi$ , induced by  $\delta_y$  near zero energy. Equation (42) reproduces the exact  $\Delta\phi$  over a relatively wide energy range. For normal incidence with  $k_y = 0$ , the phase  $\phi$  is locked to either 0 or  $\pi$  within the continuum bands, whereas inside the gap it is no longer restricted to these values.

## VIII. EXPERIMENTAL IMPLICATIONS

The phase and damping time of shear vibrations have been measured using pump-probe optical techniques [44]. Such shear vibrations can be driven by pump light with frequencies of several hundred THz. Moreover, the direction of the shear vibration can be controlled by the polarization direction of the pump light [89]. Motivated by these reports and by the results of the present work, we propose an experiment that converts the oscillating electric field of probe light into a dc current  $I_x$ , as schematically illustrated in Fig. 1 (c). First, a shear vibration along the  $y$  direction is excited by the pump pulse in the mono-bi-mono junction. On the time scale of several picoseconds, this excitation can be regarded as instantaneous. Next, a probe pulse with polarization along the  $x$  direction, resonant with the shear vibration, arrives with a delay time. The external field associated with the probe light induces an oscillation of the electron probability flow  $I_x^{(0)}$  in the monolayer regions. When  $I_x^{(0)}$  oscillates in phase with  $\delta_y$ , electrons move preferentially in the positive  $x$  direction during the high-transmission phase corresponding to  $\delta_y > 0$ , resulting in a positive time-averaged current  $I_x$ . In contrast, when  $I_x^{(0)}$  and  $\delta_y$  oscillate out of phase, the resulting dc current  $I_x$  becomes negative. The amplitudes and relative phase between  $\delta_y$  and  $I_x^{(0)}$  can be controlled by the intensities of the pump

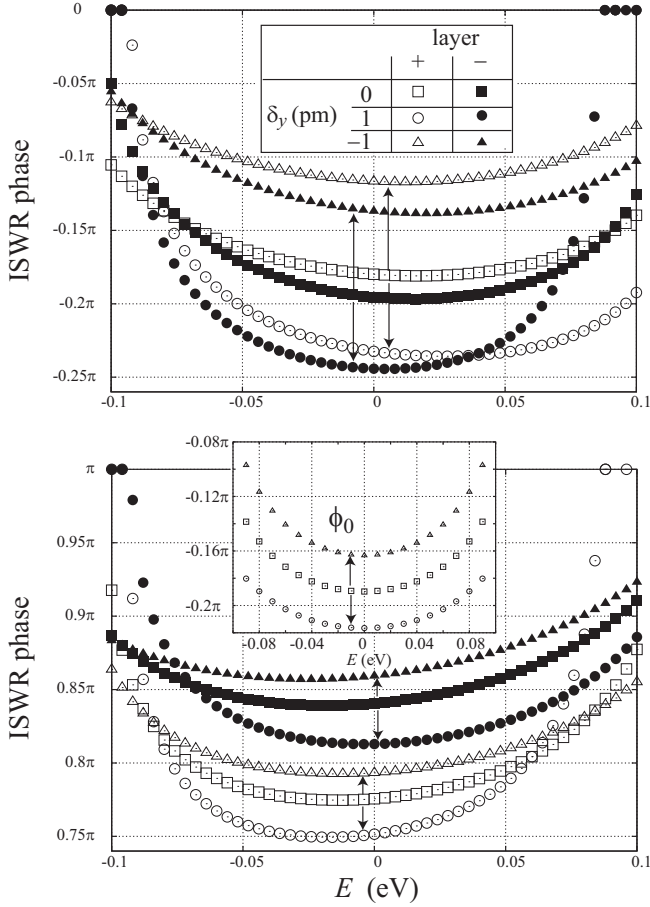


FIG. 10. The exact ISWR phase  $\phi$  for  $\delta_x = 0$ ,  $k_y = 0$ ,  $\varepsilon = 0.15$  eV in the range  $-0.26\pi < \phi \leq 0$  (top panel) and  $0.74\pi < \phi \leq \pi$  (bottom panel). Inset:  $\phi_0 = \arg[\exp(-i\theta)/\sqrt{p+iq}]$ . See the text for the definitions of  $\theta$ ,  $p$ , and  $q$ .

and probe pulses as well as by the delay time. In the absence of optical excitation, the system is symmetric under reversal of the  $x$  axis, and both the lattice displacement and the driving field that break this symmetry have zero time averages. The proposed experiment therefore provides a direct way to address whether a dc current can be generated purely by dynamical effects.

The present mechanism is closely related to quantum pumping, in which a dc current arises from cyclic modulation of system parameters without an applied bias [90–93]. However, unlike conventional pumping schemes based on gate voltages or magnetic fields, the dc current proposed here is generated solely through the controlled phase relation between dynamically driven lattice shear and the probe-induced electronic response. This distinguishes the present effect from photogalvanic and ratchet effects, which primarily rely on static spatial asymmetry or optical nonlinearities [94–98]. The proposed dc current generation is closely related to the phase delay associated with electron transmission through the bilayer barrier. Since this phase delay is connected to various

definitions of tunneling time, the effect may provide indirect information on dynamical aspects of tunneling transport [99, 100].

## IX. SUMMARY AND PERSPECTIVE

In summary, we have investigated the evanescent electronic states of AB-stacked bilayer graphene under a perpendicular electric field, focusing on low-energy states near the charge neutrality point while allowing for an interlayer bias comparable to the dominant interlayer hopping energy. Using a full tight-binding model that incorporates the interlayer hopping parameters  $\gamma_1$ ,  $\gamma_3$ , and  $\gamma_4$ , we analyzed the Bloch factor  $\lambda$  inside the electrically induced gap beyond the regime accessible to conventional low-energy analytical approaches. By approximately solving the secular equation for  $\lambda$  in terms of the complex wave number  $\xi$ , we showed that the  $\tilde{\Delta}\xi$  approximation accurately captures the behavior of evanescent modes over most of the gap, except in the immediate vicinity of the gap edges. The transport direction was chosen along the zigzag ( $x$ ) direction, with a generally complex  $k_x$  and a real transverse wave number  $k_y$ , and the solutions were classified according to the  $\lambda(k_y) - (\lambda^*(k_y))^{-1}$  symmetry, together with the signs of the real and imaginary parts of  $\xi$ .

For a mono–bi–mono junction, we found that the conductance  $G$  along the transport direction becomes insensitive to the displacement  $\delta_x$ , whereas it exhibits a positive response to  $\delta_y$ , satisfying  $dG/d\delta_y > 0$  for sufficiently thick bilayer regions. Here, the positive direction of  $\delta_y$  corresponds to the orientation where the angle between the  $\gamma_1$  bond and the in-plane  $\gamma_0$  bond on the  $yz$  plane is obtuse. This behavior is captured by the  $\tilde{\Delta}\xi$  approximation through an analytic connection between the CDL and RDL, while its breakdown near the gap edge is remedied by the complementary  $\tilde{\Delta}E$  approximation. Together, these results clarify that the effect of  $\delta_y$  originates from the  $\gamma_3$ -induced interlayer coupling. For the in-plane sublattice wave-function ratio, we also found good agreement between the  $\tilde{\Delta}\xi$  approximation and the exact numerical results. The phase  $\theta$  proportional to  $\delta_y$  plays a central role in governing these behaviors. Based on these findings, we have proposed an experimental scheme combining a mono–bi–mono junction with pump–probe optical techniques to generate a dc current from an optically driven oscillating electric field. More broadly, the present results demonstrate that a dc transport response can emerge from dynamically controlled phase relations in evanescent transport regimes between lattice motion and electronic dynamics, even in systems that preserve static spatial symmetries. While the present analysis focuses on bilayer graphene, the analytical framework developed here can in principle be extended to other layered two-dimensional materials and to transport along more general crystallographic directions, which remains an open problem for future studies.

## Appendix A: Interdependence of $\xi$ , $\tilde{k}_x$ , $\lambda$ , and $k_x$

In the present paper, we measure the wave number  $k_x$  from the  $\Gamma$  point. Contrary, the effective theory utilizes  $\tilde{k}_x$  measured from the  $K$  and  $K'$  corner points ( $k_x a = \mp 4\pi/3$ ). They are related as

$$k_x a = \tilde{k}_x a \pm \frac{2}{3}\pi \mp 2\pi, \quad (\text{A1})$$

where the upper (lower) signs correspond to the  $K$  ( $K'$ ) valley. When  $\tilde{k}_x$  is close to zero, the Bloch factor  $\lambda = \exp(ik_x a/2)$  is approximated as

$$\lambda = e^{\mp i2\pi/3} e^{i\tilde{k}_x a/2} \quad (\text{A2})$$

$$\simeq \left( -\frac{1}{2} \mp i\frac{\sqrt{3}}{2} \right) \left( 1 + i\frac{\tilde{k}_x a}{2} \right) \quad (\text{A3})$$

followed by

$$\xi \simeq \pm \sqrt{3}\tilde{k}_x a/2. \quad (\text{A4})$$

When  $\xi^i = 0$ , Eq. (19) is trivial. We consider the case where  $\xi^i \neq 0$  below. Neglecting the  $\xi^2$  order term in Eq. (16), we obtain an approximate formula

$$\begin{aligned} \sqrt{\left(\frac{\xi-1}{2}\right)^2 - 1} &= \sqrt{-\frac{3}{4} - \frac{\xi}{2} + \frac{\xi^2}{4}} \\ &\simeq \frac{\sqrt{3}}{2} \sqrt{-1 - \frac{2}{3}\xi^r - \frac{2}{3}i\xi^i}. \end{aligned} \quad (\text{A5})$$

In the square root

$$\sqrt{A} = \exp(i\varphi/2)\sqrt{|A|} \quad (\text{A6})$$

of a complex number  $A = |A|\exp(i\varphi)$ , we define the range of the phase  $\varphi$  as  $-\pi < \varphi \leq \pi$ . Under this standard definition,

$$\sqrt{-1 + o_1 + io_2} \simeq \frac{|o_2|}{2} + \text{sgn}(o_2)i \left( 1 - \frac{o_1}{2} \right) \quad (\text{A7})$$

holds for real numbers  $o_1$  and  $o_2$  when  $|o_1|, |o_2| \ll 1$ . Using Eqs. (A5) and (A7) in Eq. (16), we obtain Eq. (18). Substitution of Eq. (A4) into Eq. (A2) yields

$$\lambda = e^{\mp i\left(\frac{2}{3}\pi - \frac{\xi^r}{\sqrt{3}}\right)} e^{\mp \frac{\xi^i}{\sqrt{3}}}. \quad (\text{A8})$$

Equation (18) reduces to Eq. (A8) when  $\sigma \text{sgn}(\xi^i)$  is chosen to be positive in the  $K$  valley and negative in the  $K'$  valley.

## Appendix B: Numerical methods

In this Appendix, we summarize the method of the exact numerical calculation, which is identical to that used in Ref. [84], but rewritten in a form suitable for the

present work. To avoid confusion with other sign-related indices, we denote the lower (+) and upper (−) layers by  $\downarrow$  and  $\uparrow$ , respectively, and the central bilayer region by bi. The tight-binding equations for the corresponding periodic systems can be written in the unified form

$$E\vec{d}_j^{(\diamond)} = \sum_{\Delta j=-1}^1 h_\diamond^{(\Delta j)} \vec{d}_{j+\Delta j}^{(\diamond)}. \quad (\text{B1})$$

Here,  $\diamond = \text{bi}$  labels the bilayer region, while  $\diamond = \downarrow, \uparrow$  label the monolayer sectors. Although the  $\uparrow$  layer exists only in the bilayer region, the corresponding periodic monolayer system is introduced for notational consistency. The integer  $j$  labels the atomic position  $x = aj/2$ . In this Appendix, the exact Bloch factor  $\exp(ik_x a)$  is denoted by  $\lambda$ , while  $\tilde{\lambda}$  represents the corresponding quantity obtained within the  $\tilde{\Delta}\xi$  approximation. For the monolayer region, the exact Bloch factor  $\tilde{\Omega}$  is employed.

The Hamiltonian of the periodic bilayer system is given by

$$h_{\text{bi}}^{(\Delta j)} = \begin{pmatrix} h_{\downarrow}^{(\Delta j)} & W^{(\Delta j)} \\ {}^t(W^{(-\Delta j)})^* & h_{\uparrow}^{(\Delta j)} \end{pmatrix}, \quad (\text{B2})$$

where  $W$  is determined by the interlayer hopping. Although  $h_{\downarrow}^{(-1)} = h_{\downarrow}^{(1)}$  and  $h_{\uparrow}^{(-1)} = h_{\uparrow}^{(1)}$ ,  $W^{(-1)} \neq W^{(1)}$  when  $\delta_x \neq 0$ . Since  $k_y$  is fixed throughout the calculation,  $h_{\text{bi}}$  is represented by a  $4 \times 4$  matrix, while  $h_{\downarrow}$  is a  $2 \times 2$  matrix. The relation between Eqs. (5) and (B2) is given by

$$H = h_{\text{bi}}^{(0)} + \lambda h_{\text{bi}}^{(1)} + \frac{1}{\lambda} h_{\text{bi}}^{(-1)}. \quad (\text{B3})$$

From Eq. (B1), the transfer matrix is obtained as

$$\Gamma_\diamond = \begin{pmatrix} h_\diamond^{(1)} & 0 \\ h_\diamond^{(0)} - E & h_\diamond^{(1)} \end{pmatrix}^{-1} \begin{pmatrix} -h_\diamond^{(-1)} & E - h_\diamond^{(0)} \\ 0 & -h_\diamond^{(-1)} \end{pmatrix}. \quad (\text{B4})$$

By diagonalizing this matrix, the eigenvalues and eigenvectors are obtained as

$$\Gamma_{\text{bi}} \begin{pmatrix} \vec{u}_n \\ \vec{\lambda}_n \vec{u}_n \end{pmatrix} = \bar{\lambda}_n^2 \begin{pmatrix} \vec{u}_n \\ \vec{\lambda}_n \vec{u}_n \end{pmatrix}, \quad (\text{B5})$$

$$\Gamma_{\downarrow} \begin{pmatrix} \vec{v}_n \\ \vec{\tilde{\Omega}}_n \vec{v}_n \end{pmatrix} = \tilde{\Omega}_n^2 \begin{pmatrix} \vec{v}_n \\ \vec{\tilde{\Omega}}_n \vec{v}_n \end{pmatrix}. \quad (\text{B6})$$

When  $|\tilde{\Omega}_n| = 1$ , the eigenvector of  $\Gamma_{\downarrow}$  is normalized so that it carries unit probability current, i.e.,

$$\text{Im}\left(\tilde{\Omega}_n^* {}^t \vec{v}_n^* h_{\downarrow}^{(1)} \vec{v}_n\right) = \pm 1.$$

The exact value of  $k_x a$  is obtained from the relation  $\exp(ik_x a) = \bar{\lambda}_n^2$ .

We construct the matrices

$$\begin{pmatrix} U_{\downarrow} \\ U_{\uparrow} \end{pmatrix} = (\vec{u}_1, \vec{u}_2, \dots, \vec{u}_8), \quad (\text{B7})$$

$$V = (\vec{v}_1, \vec{v}_2), \quad (\text{B8})$$

where  $\vec{v}_1$  and  $\vec{v}_2$  correspond to modes with positive probability current. We also define diagonal matrices  $\Lambda = \text{diag}(\bar{\lambda}_1, \bar{\lambda}_2, \dots, \bar{\lambda}_8)$  and  $\Omega = \text{diag}(\tilde{\Omega}_1, \tilde{\Omega}_2)$ , together with the following matrices:

$$Y_L = - \begin{pmatrix} (U_\downarrow + g^{(+)}U_\uparrow) \Lambda \\ U_\downarrow \\ U_\uparrow \end{pmatrix}, \quad (\text{B9})$$

$$Z_L = \begin{pmatrix} V\Omega \\ V \\ 0 \end{pmatrix}, \quad (\text{B10})$$

$$Y_R = - \begin{pmatrix} U_\downarrow + g^{(-)}U_\uparrow \\ U_\downarrow \Lambda \\ U_\uparrow \Lambda \end{pmatrix} \Lambda^{N-1}, \quad (\text{B11})$$

$$Z_R = \begin{pmatrix} V \\ V\Omega \\ 0 \end{pmatrix}, \quad (\text{B12})$$

and

$$g^{(\pm)} = \frac{1}{h_\downarrow^{(\pm 1)}} W^{(\pm 1)}. \quad (\text{B13})$$

The contribution to the conductance from a given  $k_y$ , evaluated using the Landauer formula, is then obtained as

$$G_{k_y} = \frac{2e^2}{h} \sum_{n=1}^2 \sum_{n'=1}^2 |S_{n+2, n'}|^2. \quad (\text{B14})$$

Here,

$$S = \begin{pmatrix} Z_L^* & 0 & Y_L \\ 0 & Z_R & Y_R \end{pmatrix}^{-1} \begin{pmatrix} Z_L & 0 \\ 0 & Z_R^* \end{pmatrix}. \quad (\text{B15})$$

By summing Eq. (B14) over all  $k_y$  satisfying  $|\tilde{\Omega}_n| = 1$ , the total conductance  $G$  is obtained. Figure 7 (a) shows the exact conductance  $G$  calculated in this manner. Figure 7 (b) presents the result obtained by replacing  $\bar{\lambda}_n$  as

$$\bar{\lambda}_n \Rightarrow \begin{cases} \lambda_{\tau, l}, & \dots |\bar{\lambda}_n| < 1, \\ 1/(\lambda_{\tau, -l}^*) & \dots |\bar{\lambda}_n| > 1, \end{cases} \quad (\text{B16})$$

while Fig. 7 (c) shows the result obtained using the replacement

$$\bar{\lambda}_n \Rightarrow \begin{cases} \lambda_{\tau, l}/|\lambda_{\tau, l}|, & \dots |\bar{\lambda}_n| < 1, \\ |\lambda_{\tau, -l}|/(\lambda_{\tau, -l}^*), & \dots |\bar{\lambda}_n| > 1, \end{cases} \quad (\text{B17})$$

where  $\lambda$  is defined within the  $\tilde{\Delta}\xi$  approximation. Here, we determine the correspondence between  $n$  and  $(\tau, l)$  assuming  $\text{sgn}(\xi^r) = \text{sgn}(\text{Re}(\xi^{(0)})) = -\tau$ ,  $\text{sgn}(\xi^i) = \text{sgn}(\text{Im}(\xi^{(0)})) = -\tau l$ , with the relation  $\xi = 1 + \lambda + (1/\bar{\lambda})$ .

- 
- [1] S. Datta, *Electronic Transport in Mesoscopic Systems* (Cambridge University Press, Cambridge, 1995).
- [2] T. Ando, Quantum point contacts in magnetic fields, *Phys. Rev. B* **44**, 8017 (1991).
- [3] Y.-C. Chang and J. N. Schulman, Complex band structures of crystalline solids: An eigenvalue method, *Phys. Rev. B* **25**, 3975 (1982).
- [4] J. K. Tomfohr and O. F. Sankey, Complex band structure, decay lengths, and Fermi level alignment in simple molecular electronic systems, *Phys. Rev. B* **65**, 245105 (2002).
- [5] C.-S. Park, Band-Gap tuned oscillatory conductance in bilayer graphene n-p-n junction, *J. Appl. Phys.* **116**, 033702 (2014).
- [6] N. Benlakhoy, A. El Mouhafid, and A. Jellal, Transport properties in gapped bilayer graphene, *Physica E* **34**, 114835 (2021).
- [7] E. McCann, Asymmetry gap in the electronic band structure of bilayer graphene, *Phys. Rev. B* **74**, 161403(R) (2006).
- [8] J. Ruseckas, G. Juzeliūnas, and I. V. Zozoulenko, Spectrum of electrons in bilayer graphene nanoribbons and nanotubes: An analytical approach, *Phys. Rev. B* **83**, 035403 (2011).
- [9] J. Nilsson, A. H. Castro Neto, F. Guinea, and N. M. R. Peres, Electronic properties of bilayer and multilayer graphene, *Phys. Rev. B* **78**, 045405 (2008).
- [10] T. Ohta, A. Bostwick, T. Seyller, K. Horn, E. Rotenberg, Controlling the electronic structure of bilayer graphene, *Science* **313**, 951 (2006).
- [11] J. Yin, C. Tan, D. Barcons-Ruiz, I. Torre, K. Watanabe, T. Taniguchi, J. C. W. Song, J. Hone, and F. H. L. Koppens, Tunable and giant valley-selective Hall effect in gapped bilayer graphene, *Science* **375**, 1398 (2022).
- [12] J. Yan and M. S. Fuhrer, Charge transport in dual gated bilayer graphene with Corbino geometry, *Nano Lett* **10**, 4521 (2010).
- [13] K. F. Mak, C. H. Lui, J. Shan, and T. F. Heinz, Observation of an electric-field-induced band gap in bilayer graphene by infrared spectroscopy., *Phys. Rev. Lett.* **102**, 256405 (2009).
- [14] Y. Zhang, T. T. Tang, C. Girit, Z. Hao, M. C. Martin, A. Zettl, M. F. Crommie, Y. R. Shen, and F. Wang, Direct observation of a widely tunable bandgap in bilayer graphene, *Nature* **459**, 820 (2009).
- [15] R. Tamura, Tunnel valley current filter in the partially overlapped graphene under the vertical electric field, *J. Phys. Soc. Jpn.* **92**, 123704 (2023).
- [16] R. Tamura, Energy symmetry and interlayer wave function ratio of tunneling electrons in partially overlapped graphene, *Phys. Rev. B* **111**, 245436 (2025).
- [17] R. Tamura, Origins of valley current reversal in par-

- tially overlapped graphene layers, *J. Phys. Soc. Jpn.* **92**, 114706 (2023).
- [18] J. Zheng, P. Guo, Z. Ren, Z. Jiang, J. Bai, and Z. Zhang, Conductance fluctuations as a function of sliding motion in bilayer graphene nanoribbon junction: A first-principles investigation, *Appl. Phys. Lett.* **101**, 083101 (2012).
- [19] C. J. Páez, A. L. C. Pereira, J. N. B. Rodrigues, and N. M. R. Peres, Electronic transport across linear defects in graphene, *Phys. Rev. B* **92**, 045426 (2015).
- [20] J. Nilsson, A. H. Castro Neto, F. Guinea, and N. M. R. Peres, Transmission through a biased graphene bilayer barrier, *Phys. Rev. B* **76**, 165416 (2007).
- [21] K. M. M. Habib, F. Zahid, and R. K. Lake, Negative differential resistance in bilayer graphene nanoribbons, *Appl. Phys. Lett.* **98**, 192112 (2011).
- [22] E. Cannavò, D. Marian, E. G. Marín, G. Iannaccone, and G. Fiori, Transport properties in partially overlapping van der Waals junctions through a multiscale investigation, *Phys. Rev. B* **104**, 085433 (2021).
- [23] Y. Wang, Transfer matrix theory of monolayer graphene/bilayer graphene heterostructure superlattice, *J. Appl. Phys.* **116**, 164317 (2014).
- [24] D. Valencia, J.-Q. Lu, J. Wu, F. Liu, F. Zhai, and Y.-J. Jiang, Electronic transmission in Graphene suppressed by interlayer interference, *AIP Advances* **3**, 102125 (2013).
- [25] V. Torres, D. Faria, and A. Latgé, Exploring valley polarized transport in graphene bilayer flakes, *Physica B* **666**, 415148 (2023).
- [26] N. Benlakhrouy, A. Jellal, and M. Schreiber, Transport properties of hybrid single-bilayer graphene interfaces in a magnetic field, *Phys. Rev. B* **108**, 245419 (2023).
- [27] N. Benlakhrouy and A. Jellal, Tunneling conductance of hybrid bilayer-single graphene junctions, *Phys. Scr.* **99**, 075920 (2024).
- [28] D. Yin, W. Liu, X. Li, L. Geng, X. Wang, and P. Huai, Mono-bi-monolayer graphene junction introduced quantum transport channels, *Appl. Phys. Lett.* **103**, 173519 (2013).
- [29] H. Z. Olyaei, P. Ribeiro, and E. V. Castro, Transmission across a bilayer graphene region, *Phys. Rev. B* **99**, 205436 (2019).
- [30] R. Li, Z. Lin, and K. S. Chan, Intervalley conversion in bilayer-monolayer graphene junctions, *Physica E* **113**, 109 (2019).
- [31] H. M. Abdullah, B. V. Duppen, M. Zarenia, H. Bahlouli, and F. M. Peeters, Quantum transport across van der Waals domain walls in bilayer graphene, *Journal of Physics: Condensed Matter* **29**, 425303 (2017).
- [32] J. W. González, H. Santos, E. Prada, L. Brey, and L. Chico, Gate-controlled conductance through bilayer graphene ribbons, *Phys. Rev. B* **83**, 205402 (2011).
- [33] J. W. González, H. Santos, M. Pacheco, L. Chico, and L. Brey, Electronic transport through bilayer graphene flakes, *Phys. Rev. B* **81**, 195406 (2010).
- [34] B. V. Duppen and F. M. Peeters, Four-band tunneling in bilayer graphene, *Phys. Rev. B* **87**, 205427 (2013).
- [35] F. Zhang, A. H. MacDonald, and E. J. Mele, Valley Chern numbers and boundary modes in gapped bilayer graphene, *Proc. Natl. Acad. Sci.* **110**, 10546 (2013).
- [36] J. M. B. Lopes dos Santos, N. M. R. Peres, and A. H. Castro Neto, Graphene bilayer with a twist: Electronic structure, *Phys. Rev. Lett.* **99**, 256802 (2007).
- [37] R. Bistritzer and A. H. MacDonald, Moiré bands in twisted double-layer graphene, *Proc. Natl. Acad. Sci. USA* **108**, 12233 (2011).
- [38] A. Ramires and J. L. Lado, Electrically tunable gauge fields in tiny-angle twisted bilayer graphene, *Phys. Rev. Lett.* **121**, 146801 (2018).
- [39] G. Tarnopolsky, A. J. Kruchkov, and A. Vishwanath, Origin of magic angles in twisted bilayer graphene, *Phys. Rev. Lett.* **122**, 106405 (2019).
- [40] E. McCann and V. I. Fal'ko, Landau-level degeneracy and quantum Hall effect in a graphite bilayer, *Phys. Rev. Lett.* **96**, 086805 (2006).
- [41] M. Koshino and E. McCann, Trigonal warping and Berry's phase  $N\pi$  in ABC-stacked multilayer graphene, *Phys. Rev. B* **80**, 165409 (2009).
- [42] E. McCann and M. Koshino, The electronic properties of bilayer graphene, *Rep. Prog. Phys.* **76**, 056503 (2013).
- [43] P. H. Tan, W. P. Han, W. J. Zhao, Z. H. Wu, K. Chang, H. Wang, Y. F. Wang, N. Bonini, N. Marzari, N. Pugno, G. Savini, A. C. Ferrari, and A. H. Castro Neto, The shear mode of multilayer graphene, *Nat. Mater.* **11**, 294 (2012).
- [44] D. Boschetto, L. Malard, C. H. Lui, K. F. Mak, Z. Li, H. Yan, and T. F. Heinz, Real-time observation of interlayer vibrations in bilayer and few-Layer Graphene, *Nano Lett.* **13**, 4620 (2013).
- [45] M.-L. Lin, J.-B. Wu, X.-L. Liu and P.-H. Tan, Probing the shear and layer breathing modes in multilayer graphene by Raman spectroscopy, *J. Raman Spectrosc.* **49**, 19 (2018).
- [46] A. H. Castro Neto, F. Guinea, N. M. R. Peres, K. S. Novoselov, and A. K. Geim, The electronic properties of graphene, *Rev. Mod. Phys.* **81**, 109 (2009).
- [47] H. Suzuura and T. Ando, Phonons and electron-phonon scattering in carbon nanotubes, *Phys. Rev. B* **65**, 235412 (2002).
- [48] K. Sasaki, S. Murakami and R. Saito, Gauge field for edge state in graphene, *J. Phys. Soc. Jpn.* **75**, 074713 (2006).
- [49] F. Guinea, M. I. Katsnelson, and A. K. Geim, Energy gaps and a zero-field quantum Hall effect in graphene by strain engineering, *Nat. Phys.* **6**, 30 (2010).
- [50] M. A. H. Vozmediano, M. I. Katsnelson, and F. Guinea, Gauge fields in graphene, *Phys. Rep.* **496**, 109 (2010).
- [51] P. San-Jose, J. González, and F. Guinea, Non-Abelian gauge potentials in graphene bilayers, *Phys. Rev. Lett.* **108**, 216802 (2012).
- [52] Y.-W. Son, S.-M. Choi, Y. P. Hong, S. Woo, and S.-H. Jhi, Electronic topological transition in sliding bilayer graphene *Phys. Rev. B* **84**, 155410 (2011).
- [53] K. W. Lee, and C. E. Lee, Extreme sensitivity of the electricfield-induced band gap to the electronic topological transition in sliding bilayer graphene, *Sci. Rep.* **5**, 17490 (2015).
- [54] M. Fujita, K. Wakabayashi, K. Nakada, and K. Kusakabe, *J. Phys. Soc. Jpn.* **65**, 1920 (1996).
- [55] S. Tapar and B. Muralidharan, Effectuating tunable valley selection via multiterminal monolayer graphene devices, *Phys. Rev. B* **107**, 205415 (2023).
- [56] W. Yao, S. A. Yang, and Q. Niu, Edge states in graphene: From gapped flat-band to gapless chiral modes, *Phys. Rev. Lett.* **102**, 096801 (2009).
- [57] V. S. Prudkovski, Y. Hu, K. Zhang, Y. Hu, P. Ji, G. Nunn, J. Zhao, C. Shi, A. Tejada, D. Wander, A. D.

- Cecco, C. B. Winkelmann, Y. Jiang, T. Zhao, K. Wakabayashi, Z. Jiang, L. Ma, C. Berger, and W. A. de Heer, An epitaxial graphene platform for zero-energy edge state nanoelectronics, *Nat. Commun.* **13**, 7814 (2022).
- [58] J. Li, I. Martin, M. Büttiker, and A. F. Morpurgo, Topological origin of subgap conductance in insulating bilayer graphene, *Nat. Phys.* **7**, 38 (2011).
- [59] E. V. Castro, N. M. R. Peres, J. M. B. Lopes dos Santos, A. H. Neto, and F. Guinea, Localized states at zigzag edges of bilayer graphene, *Phys. Rev. Lett.* **100**, 026802 (2008).
- [60] K. Davydov, X. Zhang, W. Ren, M. Coles, L. Kline, B. Zucker, K. Watanabe, T. Taniguchi, and K. Wang, Easy-to-configure zero-dimensional valley-chiral modes in a graphene point junction, *Sci. Adv.* **10**, eadp6296 (2024).
- [61] Z. Qiao, J. Jung, Q. Niu, and A. H. MacDonald, Electronic highways in bilayer graphene, *Nano Lett.* **11**, 3453 (2011).
- [62] I. Martin, Y. M. Blanter, and A. F. Morpurgo, Topological confinement in bilayer graphene, *Phys. Rev. Lett.* **100**, 036804 (2008).
- [63] J. Jung, F. Zhang, Z. Qiao, and A. H. MacDonald, Valley-Hall kink and edge states in multilayer graphene, *Phys. Rev. B* **84**, 075418 (2011).
- [64] S.-g. Cheng, H. Liu, H. Jiang, Q.-F. Sun, and X. C. Xie, Manipulation and characterization of the valley-polarized topological kink states in graphene-based interferometers, *Phys. Rev. Lett.* **121**, 156801 (2018).
- [65] H. Chen, P. Zhou, J. Liu, J. Qiao, B. Oezylmaz, and J. Martin, Gate controlled valley polarizer in bilayer graphene, *Nat. Commun.* **11**, 1202 (2020).
- [66] J. Li, K. Wang, K. J. McFaul, Z. Zern, Y. Ren, K. Watanabe, T. Taniguchi, Z. Qiao, and J. Zhu, Gate-controlled topological conducting channels in bilayer graphene, *Nat. Nanotechnol.* **11**, 1060 (2016).
- [67] J. Lee, K. Watanabe, T. Taniguchi, H.-J. Lee, Realisation of topological zero-energy mode in bilayer graphene in zero magnetic field, *Sci. Rep.* **7**, 6466 (2017).
- [68] F. Zhang, A. H. MacDonald, and E. J. Mele, Valley Chern numbers and boundary modes in gapped bilayer graphene, *Proc. Natl. Acad. Sci.* **110**, 10546 (2013).
- [69] L.-J. Yin, H. Jiang, J.-B. Qiao, and L. He, Direct imaging of topological edge states at a bilayer graphene domain wall, *Nat. Commun.* **7**, 11760 (2016).
- [70] L. Ju, Z. Shi, N. Nair, Y. Lv, C. Jin, J. Velasco, C. Ojeda-Aristizabal, H. A. Bechtel, M. C. Martin, A. Zettl, J. Analytis, and F. Wang, Topological valley transport at bilayer graphene domain walls, *Nature* **520**, 650 (2015).
- [71] F. R. Geisenhof, F. Winterer, A. M. Seiler, J. Lenz, I. Martin, R. T. Weitz, Interplay between topological valley and quantum Hall edge transport, *Nat. Commun.* **13**, 4187 (2022).
- [72] F. R. Geisenhof, F. Winterer, S. Wakolbinger, T. D. Gokus, Y. C. Durmaz, D. Priesack, J. Lenz, F. Keilmann, K. Watanabe, T. Taniguchi, R. Guerrero-Avilés, M. Pelc, A. Ayuela, and R. T. Weitz, Anisotropic strain-induced soliton movement changes stacking order and band structure of graphene multilayers: Implications for charge transport, *ACS Appl. Nano Mater.* **2**, 6067 (2019).
- [73] J. Pan, H. Wang, L. Zou, X. Wang, L. Zhang, X. Dong, H. Xie, Y. Ding, Y. Zhang, T. Taniguchi, K. Watanabe, S. Wang, and Z. Wang, Topological valley transport in bilayer graphene induced by interlayer sliding, *Phys. Rev. Lett.* **135**, 126603 (2025).
- [74] G. W. Semenoff, V. Semenoff, and F. Zhou, Domain walls in gapped graphene, *Phys. Rev. Lett.* **101**, 087204 (2008).
- [75] S.-g. Cheng, J. Zhou, H. Jiang, and Q.-F. Sun, The valley filter efficiency of monolayer graphene and bilayer graphene line defect model, *New J. Phys.* **18**, 129601 (2016).
- [76] Ph. Lambin, V. Meunier, and A. Rubio, Electronic structure of polychiral carbon nanotubes, *Phys. Rev. B* **62**, 5129 (2000).
- [77] B. Partoens and F. M. Peeters, From graphene to graphite: Electronic structure around the K point, *Phys. Rev. B* **74**, 075404 (2006).
- [78] G. W. Semenoff, Condensed-matter simulation of a three-dimensional anomaly, *Phys. Rev. Lett.* **53**, 2449 (1984).
- [79] T. Ando, Theory of electronic states and transport in carbon nanotubes, *J. Phys. Soc. Jpn.* **74**, 777 (2005).
- [80] In Ref. [16],  $K_+$  and  $K_-$  valleys correspond to wave numbers  $k_x a = -2\pi/3$  and  $k_x a = 2\pi/3$ , respectively.
- [81] E. Durand, *Solutions numériques des équations algébriques*, Vol. 1 (Masson, Paris, 1960).
- [82] I. O. Kerner, Ein Gesamtschrittverfahren zur Berechnung der Nullstellen von Polynomen, *Numer. Math.* **8**, 290 (1966).
- [83] M. Büttiker, Y. Imry, R. Landauer, and S. Pinhas, Generalized many-channel conductance formula with application to small rings, *Phys. Rev. B* **31**, 6207 (1985).
- [84] R. Tamura, Perturbation calculations on interlayer transmission rates from symmetric to antisymmetric channels in parallel armchair nanotube junctions, *Phys. Rev. B* **99**, 155407 (2019).
- [85] From the secular equation of  $H''$ , we also obtain equations  $\phi_{\pm}'' \xi'' + (E \pm \varepsilon) \phi_{\pm}'' = 0$ . However these equations do not include the dominant interlayer hopping  $\gamma_1$  and thus ineffective in the interlayer hopping effect.
- [86] G. Tamaki, T. Kawakami, and M. Koshino, Topological junction states and their crystalline network in systems with chiral symmetry: Application to graphene nanoribbons, *Phys. Rev. B* **101**, 205311 (2020).
- [87] S. Ryu and Y. Hatsugai, Topological origin of zero-energy edge states in particle-hole symmetric systems, *Phys. Rev. Lett.* **89**, 077002 (2002).
- [88] R. Tamura, Valley current filtering and reversal by parallel side contacted armchair nanotubes, *J. Phys. Soc. Jpn.* **90**, 114701 (2021).
- [89] H. Rostami, Theory for shear displacement by light-induced Raman force in bilayer graphene, *Phys. Rev. B* **106**, 155405 (2022).
- [90] D. J. Thouless, Quantization of particle transport, *Phys. Rev. B* **27**, 6083 (1983).
- [91] P. W. Brouwer, Scattering approach to parametric pumping, *Phys. Rev. B* **58**, R10135 (1998).
- [92] M. Moskalets and M. Büttiker, Floquet scattering theory of quantum pumps, *Phys. Rev. B* **66**, 205320 (2002).
- [93] P. San-Jose, E. Prada, E. McCann, and H. Schomerus, Single-parameter pumping in graphene, *Phys. Rev. B* **84**, 155408 (2011).
- [94] V. I. Belinicher and B. I. Sturman, The photogalvanic effect in media lacking a center of symmetry, *Sov. Phys. Usp.* **23**, 199 (1980).

- [95] S. D. Ganichev and W. Prettl, Spin photocurrents in quantum wells, *J. Phys.: Condens. Matter* **15**, R935 (2003).
- [96] C. Drexler, S. A. Tarasenko, P. Olbrich, J. Karch, M. Hirmer, F. Müller, M. Gmitra, J. Fabian, R. Yakimova, S. Lara-Avila, S. Kubatkin, M. Wang, R. Vajtai, P. M. Ajayan, J. Kono, and S. D. Ganichev, Magnetic quantum ratchet effect in graphene, *Nat. Nanotechnol.* **8**, 104 (2013).
- [97] M. M. Glazov and S. D. Ganichev, High frequency electric field induced nonlinear effects in graphene, *Phys. Rep.* **535**, 101 (2014).
- [98] P. Olbrich, S. A. Tarasenko, C. Reitmaier, J. Karch, D. Plohmann, Z. D. Kvon, and S. D. Ganichev, Observation of the orbital circular photogalvanic effect *Phys. Rev. B* **79**, R121302 (2009).
- [99] R. Landauer and Th. Martin, Barrier interaction time in tunneling, *Re. Mod. Phys.* **66**, 217 (1994).
- [100] E. H. Hauge, and J. A. Støvneng, Tunneling times: a critical review, *Rev. Mod. Phys.* **61**, 917 (1989).